Paleoceanography and Paleoclimatology

RESEARCH ARTICLE
10.1029/2022PA004423

Key Points:

- ^{10}Be dating of moraines indicates at least four glacier maxima in the Mongolian Altai during the Last Glaciation
- The timing of Mongolian glacier maxima overlapped with the global Last Glacial Maximum
- Deglaciation began as early as ~18.8 kyrs ago and interglacial conditions were achieved by ~16.0 kyrs ago

Supporting Information:

Supporting Information may be found in the online version of this article.

Correspondence to:

P. D. Strand,
peter.strand@maine.edu

Citation:

Strand, P. D., Putnam, A. E., Sambuu, O., Putnam, D. E., Denton, G. H., Schaefer, J. M., et al. (2022). A ^{10}Be moraine chronology of the Last Glaciation and termination at 49°N in the Mongolian Altai of Central Asia. *Paleoceanography and Paleoclimatology*, *37*, e2022PA004423. https://doi.org/10.1029/2022PA004423

Received 24 MAR 2021
Accepted 12 APR 2022

Author Contributions:

Conceptualization: Peter D. Strand, David E. Putnam, George H. Denton, Joerg M. Schaefer
Data curation: Peter D. Strand, Daniel G. Cole
Formal analysis: Peter D. Strand, Joerg M. Schaefer
Investigation: Peter D. Strand, Oyungerel Sambuu, David E. Putnam, Mariah J. Radue, Ariunsanaa Dorj, Pagamsuren Amarsaikhan, Jessica Stevens
Resources: Oyungerel Sambuu, David E. Putnam, Mariah J. Radue
Supervision: Oyungerel Sambuu, David E. Putnam, George H. Denton
Visualization: Peter D. Strand, Daniel G. Cole
Writing – original draft: Peter D. Strand, George H. Denton, Mariah J. Radue

A ^{10}Be Moraine Chronology of the Last Glaciation and Termination at 49°N in the Mongolian Altai of Central Asia

Peter D. Strand[1], Aaron E. Putnam[1], Oyungerel Sambuu[2], David E. Putnam[3], George H. Denton[1], Joerg M. Schaefer[4], Mariah J. Radue[1], Ariunsanaa Dorj[2], Pagamsuren Amarsaikhan[2], Jessica Stevens[5], and Daniel G. Cole[6]

[1]School of Earth and Climate Sciences, Climate Change Institute, University of Maine, Orono, ME, USA, [2]School of Geology and Mining Engineering, Mongolian University of Science and Technology, Ulaanbaatar, Mongolia, [3]College of Arts and Sciences, Environmental Science and Sustainability, University of Maine at Presque Isle, Presque Isle, ME, USA, [4]Lamont-Doherty Earth Observatory, Palisades, NY, USA, [5]Gary Comer College Prep, Chicago, IL, USA, [6]Smithsonian Institution, National Museum of Natural History, Washington, DC, USA

Abstract Determining what caused the global Last Glaciation and last glacial termination, despite opposing orbital summer insolation signatures between the polar hemispheres, remains a puzzle of paleoclimatology. This problem can be addressed by comparing chronologies of glaciation from different latitudes and different climatic regimes in both hemispheres. Here, we present a ^{10}Be surface-exposure chronology of glacial landforms constructed during and since the local Last Glaciation in the continental environment of interior Asia in the high Mongolian Altai (49°N, 88°E). Four belts of lateral moraines document maximal phases of the former Khoton glacier at 35,400 ± 980 years ago, 23,430 ± 850 years ago, 20,780 ± 610 years ago, and 19,520 ± 550 years ago. Our chronology indicates that deglaciation from these maximal positions began as early as 18,810 ± 510 years ago, was well underway by 17,680 ± 510 years ago, and was nearly completed by 16,040 ± 490 years ago. Overall, our chronology shows that glaciation in western Mongolia coincided with the global Last Glacial Maximum and that extensive recession from glacial-to-interglacial limits took place rapidly early in the last glacial termination during Heinrich Stadial 1. The transition from glacial to interglacial conditions led to the demise of large Northern Hemisphere ice sheets and increase in radiative forcing agents by several millennia. We suggest that this rapid switch in the mode of glaciation implies the involvement of an additional climatic factor that could have produced locally rapid warming and deglaciation ~18,800–16,000 years ago.

Plain Language Summary Leading hypotheses for the causes of ice ages and their terminations involve important roles for ice sheet feedbacks and greenhouse gases in driving global glacial cycles. Mountain glacier length records afford valuable insight into past climate conditions because mountain glaciers are highly sensitive to the effects of atmospheric temperature changes. Here, we use glacial geology and surface-exposure dating to chart the ice-age history of a mountain glacier system located in the Mongolian Altai of Central Asia. Results from the Altai show that the ancient glacier achieved ice-age maxima at the same time as glaciers in midlatitude Southern Alps of New Zealand on the opposite side of the world. Likewise, rapid and extensive glacier recession took place in both locations between ~18,000 and 16,000 years ago—signaling an early and rapid termination of ice age conditions in these two bipolar midlatitude locations. The rapid climate warming that drove glacier retreat in western Mongolia led to the demise of the huge Northern Hemisphere ice sheets by several millennia and even outpaced the rise of atmospheric CO_2. Any solution to the ice-age climate puzzle must account for synchrony of glacial maxima as well as coeval rapid deglaciation in Central Asia and the Southern Hemisphere.

1. Introduction

A long-standing cornerstone of ice-age climate change originated when Murphy (1869) and Milankovitch (1941) both tied cool northern summers originating from orbital variations to the growth of ice-age glaciers. Indeed, changes in global ice volume, dominated by Northern Hemisphere ice sheets, exhibited frequencies consistent with orbitally induced summer seasonal insolation changes at 65°N latitude (Broecker, 1966; Broecker & van Donk, 1970; Hays et al., 1976; Imbrie & Imbrie, 1980; Roe, 2006). For example, Northern Hemisphere ice sheets achieved their Last Glacial Maximum (LGM) positions between ~26 and 19 ka (Clark et al., 2009; Clark &

Writing – review & editing: Peter D. Strand, Oyungerel Sambuu, David E. Putnam, George H. Denton, Joerg M. Schaefer, Mariah J. Radue, Ariunsanaa Dorj, Pagamsuren Amarsaikhan, Jessica Stevens, Daniel G. Cole

Mix, 2002; Mix et al., 2001), an interval of decreased summer insolation intensity at northern latitudes. Moreover, global sea level was lowest during the LGM and rose during the last termination, attributed largely to the growth and subsequent melting of the Northern Hemisphere ice sheets that accompanied decreasing and increasing northern summer insolation intensity (Lambeck et al., 2014; Peltier & Fairbanks, 2006; Raymo et al., 2006).

However, there exists a problem with the orbitally produced summer insolation driver for late Quaternary ice ages proposed by Murphy (1869) and Milankovitch (1941). Namely, this mechanism should have produced changes in ice-age glacier extents that were antiphased between middle latitudes of the two polar hemispheres due to opposing effects of orbital precession on summer insolation intensity. However, Mercer (1984) showed paradoxically that maximal glacial extent during the LGM was nearly synchronous for the Patagonian Ice Field in the Andes of South America and for the Laurentide Ice Sheet in the Great Lakes region of North America. Moreover, Mercer (1984) pointed out that the termination was generally synchronous between the polar hemispheres despite opposite patterns of insolation change. Quoting Broecker (1978), Mercer (1984) referred to such globally simultaneous climatic change as "a fly in the insolation ointment of the Milankovitch hypothesis." This problem was referred to as "Mercer's Paradox" in Denton et al. (2021).

Here, we seek to address Mercer's Paradox by evaluating the timing of the LGM and last glacial termination of mountain glaciers from ^{10}Be exposure dating of moraine systems at either end of an Australasian interhemispheric transect in the Mongolia Altai at 49°N and in the Southern Alps of New Zealand at 44°S. We present a ^{10}Be surface-exposure chronology of glacial landforms of the Khoton Nuur valley in the high Mongolian Altai (49°N, 88°E). We then compare the Mongolian chronologic record with comparable chronologies from elsewhere in Eurasia and then with those from the Southern Alps of New Zealand. In addition to being located at midlatitudes in opposite hemispheres (comparable to Mercer's interhemispheric comparison for the Americas), these glacier settings are located in distinctly different environments with the Mongolian Altai centered within Earth's largest continent and the Southern Alps of New Zealand within the Earth's largest ocean. On the basis of this comparison, we consider whether radiative forcing agents, ice-sheet feedbacks, and/or interhemispheric heat redistribution (i.e., the bipolar seesaw) were sufficient to explain the Last Glaciation and termination at these midlatitude locations. If Mercer's Paradox applies to midlatitude environments within the continental climates of interior Asia and in the maritime climatic setting of the Southern Alps, then an important problem would be to determine what factors would have produced simultaneous climatic change in the middle latitudes of both polar hemispheres under such different environmental conditions.

2. Physical Setting of the Altai Mountains

The Altai Mountains extend from the Gobi Desert to the West Siberian Plain (45–52°N to 89–94°E). They transect the political boundaries of Mongolia, China, Russia, and Kazakhstan (Figure 1). The mountains formed through subduction zone processes on the margins of the Eurasian continent as part of the Central Asian Orogenic Belt (Windley et al., 2002). The Mongolian Altai features the Tavan Bogd massif, which includes the highest peaks of the range. Local lithologies include metamorphosed quartzo-feldspathic graywacke sandstones, granites, othogneisses, and intrusive volcanics (Windley et al., 2002).

The Altai are situated near the geographical center of Eurasia, where atmospheric temperatures bear a dominant "continental" signature related to radiative heating of the interior Asian landmass (McKinnon et al., 2013). The climate of Mongolia features dramatic seasonal temperature swings with monthly mean atmospheric temperatures ranging from −30°C in winter months to +25°C in summer months, corresponding to a seasonal contrast of ∼55°C (Lehmkuhl et al., 2011). A meteorological station at 3,040 m a.s.l. near the Potanin Glacier in the Mongolian Altai recorded mean summer temperatures of 3.4°C and mean annual temperatures of −8.8°C between CE 2007 and CE 2008 (Konya et al., 2010). The Altai receive orographic precipitation from moisture transport via the boreal westerlies, leading to spatial variations in precipitation amounts. Precipitation totals are estimated to be greater than 1,000 mm annually on the high peaks of western Mongolia (Konya et al., 2013; Lehmkuhl et al., 2011, 2016; Nakazawa et al., 2012, 2015).

This region is a UNESCO World Heritage Site known for an extensive assemblage of petroglyphs pecked onto glacially molded bedrock and onto glacial erratics in the region. These petroglyphs depict the domestication of the horse, technological innovations, such as horse-drawn carts and the invention of the stirrup, and the rise of the

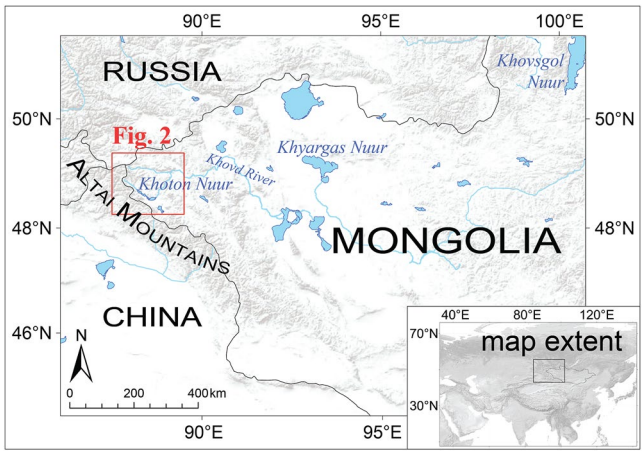

Figure 1. Topographic and political map of the western Mongolia region. Locations from the text are noted. Location of Figure 2 is outlined. Imagery from ESRI.

Mongol Empire among other important aspects of cultural and natural history of the Altai region (Fitzhugh, 2011; Jacobson-Tepfer, 2013; Kortum, 2014). Petroglyphs commonly contain rock varnish (i.e., manganese oxide coatings) within the pecked depressions. Developing an improved chronology of deglaciation in the region will afford a chronological foundation for the cultural history depicted in the rock art.

3. Climatic Significance of Mongolian Glaciers

The modern glacierized area of the entire Altai is estimated to be 1,562 km^2 (Blomdin et al., 2016). Yabuki and Ohata (2009) determined that there are ~578 present-day glaciers with an estimated total glaciated area of ~424 km^2 in the Mongolian sector of the Altai. Included is the Potanin Glacier—the largest of the Mongolian Altai (Yabuki & Ohata, 2009). Kamp and Pan (2015) calculated that the total glacierized area in Mongolia has decreased by 28% from 1990 to 2010 based on Landsat imagery analysis. Total glacierized area in the nearby Tavan Bogd massif is estimated to have decreased by ~43% since the Late Holocene (Ganiushkin et al., 2015, 2018; Lehmkuhl et al., 2011). Modern equilibrium line altitudes (ELAs) range from ~3,000 m a.s.l. in the relatively humid northwestern ranges of the Altai to ~3,700 m a.s.l. in the semiarid and arid southeastern Gobi Altai (Lehmkuhl et al., 2004, 2016).

Mountain glaciers in midlatitude climates are controlled primarily by the summer melt and therefore react quickly to atmospheric temperature changes (Anderson & Mackintosh, 2006; Anderson et al., 2010; Mackintosh et al., 2017; Oerlemans, 1994; Rupper et al., 2009; Rupper & Roe, 2008). We chose the Mongolian Altai study area specifically because glacier mass balance has been shown to be dominantly sensitive to temperature (Khalzan et al., 2022; Rupper & Roe, 2008; Rupper et al., 2009). Modern Mongolian glaciers are "summer accumulation-type glaciers," where peak ablation and mass accumulation occur simultaneously in the summer season (Khalzan et al., 2022). These types of glaciers have been identified as being particularly sensitive to atmospheric temperature changes (Ageta & Higuchi, 1984; Khalzan et al., 2022; Litt et al., 2019; Rupper et al., 2009). Khalzan et al. (2022) quantified Mongolian glacier mass-balance sensitivity to changes in temperature and precipitation and showed that an ~30% increase in precipitation would be required to offset the effects of a 1°C warming for the nearby Potanin Glacier. It is worth noting that despite being located in differing precipitation regimes, all Mongolian glaciers studied by Khalzan et al. (2022) currently exhibit negative mass balance and recession amid rising summer temperatures.

Meltwater channels, outwash deposits, and other glaciofluvial features associated with moraine complexes in the study area indicate that glaciers maintained melting ablation zones throughout the local Last Glaciation and last glacial termination (Klinge et al., 2021; Lehmkuhl et al., 2016). This observation indicates that temperature-driven surface melt has remained the dominant mode of ablation in the Mongolian Altai since the Last Glaciation as it is today (Khalzan et al., 2022). Given modern observations of strong temperature sensitivity of mountain glaciers to climate change (e.g., Hock et al., 2019; Hugonnet et al., 2021; Oerlemans, 2005; Zemp et al., 2015), we have no reason to assume that this glacier sensitivity or the seasonality of accumulation and ablation has changed markedly in the past for Altai glaciers. There are indications that the climate of Central Asia may have even been marginally wetter during the LGM (Zhang & Li, 2022; Zhang et al., 2018), which according to the mass-balance observations of Khalzan et al. (2022) and Rupper and Roe (2008) would have further reduced Mongolian glacier sensitivity to precipitation changes during that time. For these reasons, mountain glaciers in the Mongolian Altai are well situated to record regional temperature changes in the interior of the Asian continent (Khalzan et al., 2022; Rupper & Roe, 2008; Rupper et al., 2009; Surazakov et al., 2007), and we interpret the moraine chronology as reflecting changes in the past summer temperature.

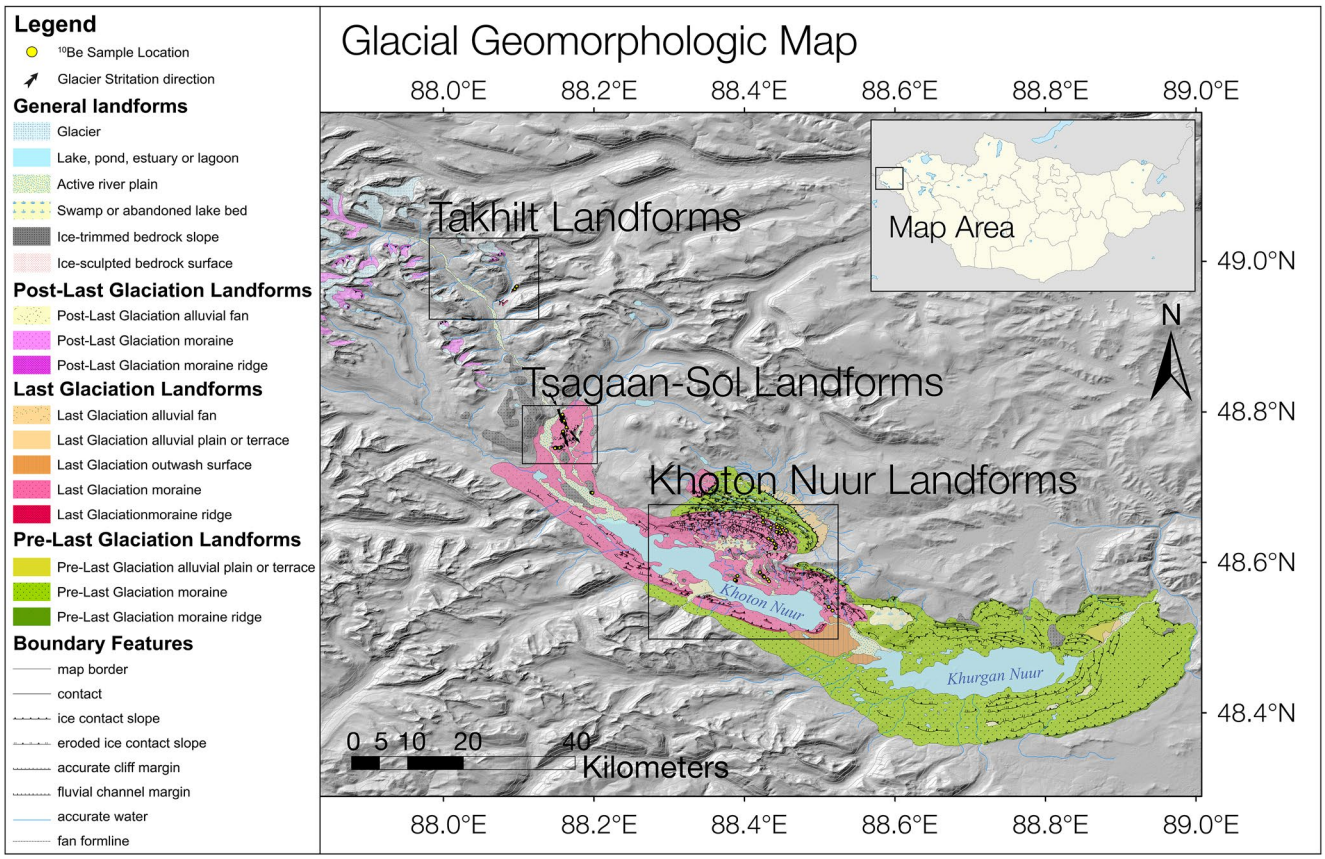

Figure 2. General glacial geomorphic map of the Khoton Nuur region of the western Mongolian Altai. Location within Mongolia is indicated within the inset map. Boxes delineate detailed map areas shown in Figure 3. Geomorphological symbols are described in legend, inset.

4. Prior Work

The timing and magnitude of Pleistocene glacier advances in the broader Altai have been the subject of prior investigations (Lehmkuhl et al., 2004, 2007, 2011, 2016; Blomdin et al., 2016; Dong et al., 2020; Gribenski et al., 2016, 2018; Klinge et al., 2021; Yang et al., 2017). A number of chronologies indicate that full-glacial configurations of Central Asian mountain glaciers were achieved not only during the global LGM in Marine Isotope Stage (MIS) 2 (~29–14 ka; Lisiecki & Raymo, 2005), but also preceding the global LGM during MIS 3 (~57–29 ka; Lisiecki & Raymo, 2005) (Batbaatar et al., 2018; Blomdin et al., 2018; Dong et al., 2020; Gillespie et al., 2008; Gribenski et al., 2016, 2018; Klinge et al., 2021; Krivonogov et al., 2012; Lehmkuhl et al., 2011; Prokopenko et al., 2009; Rother et al., 2014). Debate remains as to whether glacial advances during the local Last Glaciation were synchronous throughout Central Asia (e.g., Batbaatar et al., 2018); these issues may reflect the scarcity of well-resolved glacial chronologies or lack of landform preservation.

5. Geomorphology

During recent glaciations, the westernmost and highest part of the Mongolian Altai featured an icefield that was drained by prominent valley glaciers that extended ~50 km beyond their present-day limits. The glacier that occupied the Khoton Nuur (*Nuur* is Mongolian for *Lake*) valley during recent glacial maxima (here called the "Khoton glacier") was fed by coalescent tributaries flowing from the Tsagaan-Sol and the Tsagaan-Us valleys into a major lobe that constructed several moraines. Khoton Nuur and Khurgan Nuur (Khurgan Nuur is also known locally as *Khovd* Nuur) now occupy moraine-dammed basins within a glacially eroded trough (Figure 1). Geomorphological maps of the Khoton Nuur study area are shown in Figures 2 and 3. Photographs showing selected landforms discussed in the text are shown in Figure 4.

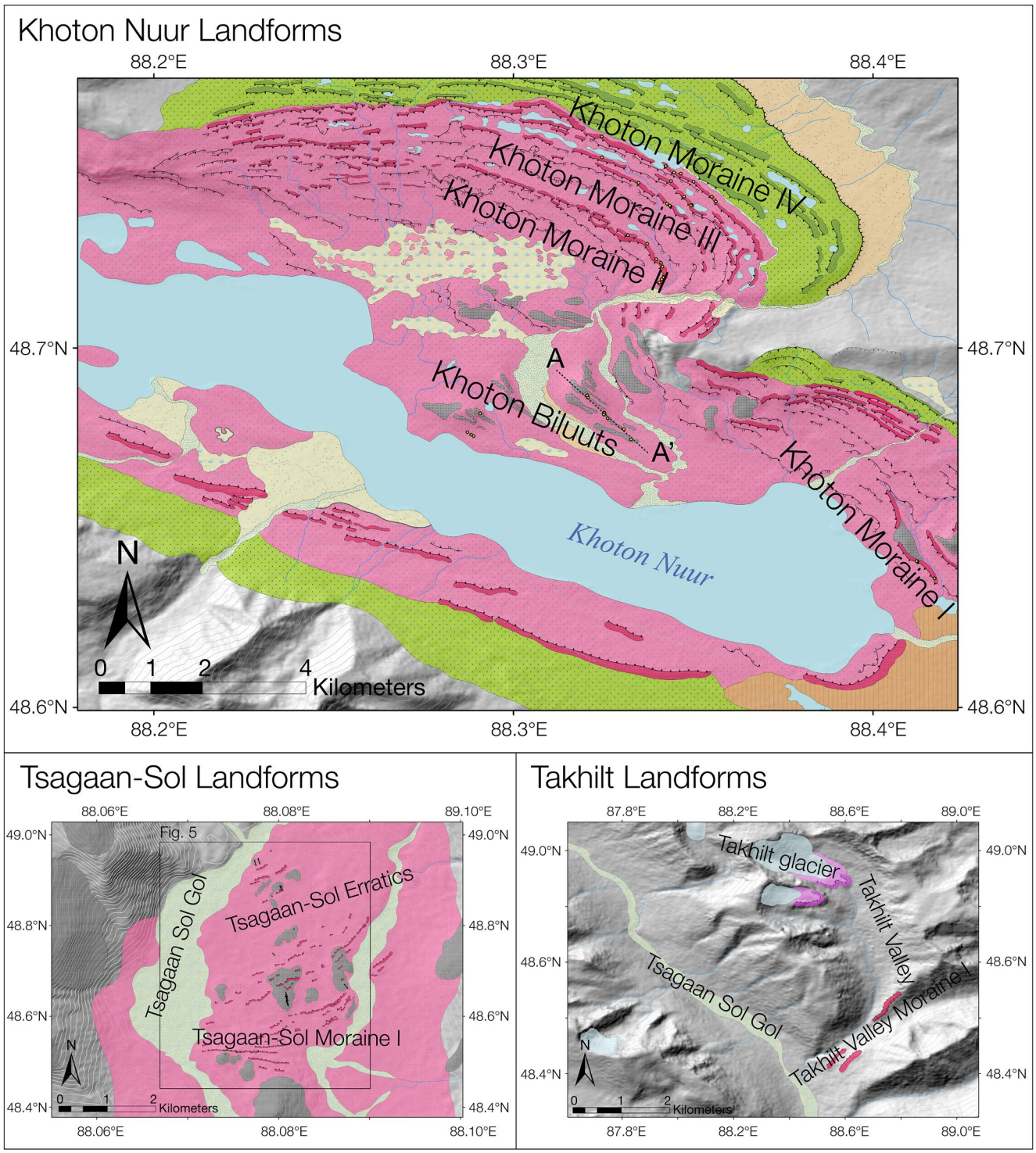

Figure 3. Detailed glacial geomorphic maps of glacial landforms in the Khoton Nuur region. Map symbols are described in Figure 2 legend.

The outermost and hence oldest glacial landforms consist of discontinuous moraine ridges and ground moraine cut by intermittent former meltwater channels that impound Khurgan Nuur—the easternmost lake of the valley. Located inboard of Khurgan Nuur is a sequence of four primary moraine belts with associated outwash plains and meltwater channels that impound Khoton Nuur. Here, we refer to the four major moraine belts in the Khoton Nuur area as (from oldest to youngest): Khoton IV, Khoton III, Khoton II, and Khoton I. Cross-cutting landform

relationships indicate that the Khoton III, Khoton II, and Khoton I landforms were constructed during the culminations of Khoton glacier advances. Inboard of the Khoton Nuur moraine complex, the landscape is dominated by ice-molded bedrock mantled in places by erratic boulders, thin glacial drift, and patches of recessional moraine ridges. About 60 km inboard of the terminal moraine that impounds Khoton Nuur is a small hanging tributary valley nestled within the high Mongolian Altai just south of Takhilt Pass (here referred to as "Takhilt Valley"). The mouth of Takhilt Valley features a boulder-rich lateral moraine that was constructed within ∼5 km of a belt of Late-Holocene moraines located at the head of the valley. This was the innermost, and hence youngest, landform that we targeted for surface-exposure dating.

6. Methods

6.1. Geomorphic Mapping

We constructed glacial geomorphologic maps to aid in the interpretation of glacial landforms and to provide context for samples collected for surface-exposure dating. Our maps were constructed in ArcGIS following the style of Andersen et al. (1999) and using the digital symbology of (Figures 2, 3 and 5). We drew upon a combination of field observations and satellite imagery analysis to interpret the landforms. Our glacial geomorphologic maps were developed using a 1-m resolution orthoimage mosaic obtained by targeted GeoEye (now DigitalGlobe) satellite photography as well as an ∼1–3 m resolution digital elevation model (DEM) determined photogrammetrically from stereo image pairs acquired from those same satellite observations. In regions outside the coverage of the GeoEye satellite imagery, we acquired high-resolution orthoimage mosaics using a DJI Phantom 4 drone and the Map Pilot software for Apple iPad. Image mosaics and DEMs (resolution ∼50 cm/px) were derived photogrammetrically from the aerial images using the Agisoft MetaShapePro software package and georeferenced using ground-control points established with differential GPS techniques (see below). Examples of drone imagery and elevation data sets are provided in Figure 5. For regions that were outside of the orthoimage mosaic coverage, we used Google Earth, ESRI imagery data sets, and Shuttle Radar Transit Mapping (SRTM) DEM as base maps.

6.2. ^{10}Be Surface Exposure Dating

Our field protocols for ^{10}Be sample collection were based on the approach of Putnam et al. (2010) and Strand et al. (2019). We targeted boulders rooted in stable positions on well-preserved moraine ridges. We also sampled erratic boulders perched or resting on bedrock surfaces to establish a chronology of glacier recession and ice-surface lowering. We avoided areas showing evidence for postdepositional modification by mass-wasting/slope processes, fluvial reworking, or human disturbance, such as road building. We selected boulders with quartz-rich lithologies, such as quartzo-feldspathic graywacke sandstones and granitoids. Boulders with steeply sloping tops, fractured/deeply pitted surfaces, or evidence of spalling were avoided as were boulders exhibiting signs of postdepositional movement. Whenever possible, we sampled from glacially polished, flat, or gently rounded top surfaces of selected boulders. Preliminary analyses from a collection of angular boulders on a moraine ridge in the Tsagaan-Sol area indicated that angular boulders are more prone to contain inherited ^{10}Be (see Section S1.2.2 in Supporting Information S1). On the basis of those results, we modified our approach to select only boulders with rounded surfaces and preserved glacial polish, indicating that the clasts had been subjected to sufficient glacial abrasion during englacial transport to remove any inherited ^{10}Be that may have accumulated as a result of prior exposure to cosmic radiation. Where possible, we sampled several boulders from each glacial landform. Examples of boulders selected and sampled for ^{10}Be exposure-age dating are shown in Figure 6.

We extracted rock samples using either quarry wedges and shims or else hammer and chisel. GPS coordinates and elevations were measured for each sample using a Trimble Geo7x GPS unit. The GPS measurements were then corrected against base-station data collected either from a fixed Trimble NetR9 unit or else from a Trimble Geo7x unit located at our field camp, generally within ∼10 km of the sample sites. Horizontal and vertical uncertainties for differentially corrected GPS measurements were typically less than ±1 m. For cases in which GPS points were unable to be differentially corrected due to incomplete or missing base data, we extracted sample elevations from a GeoEye-derived DEM (±1 m horizontal and ±3 m vertical).

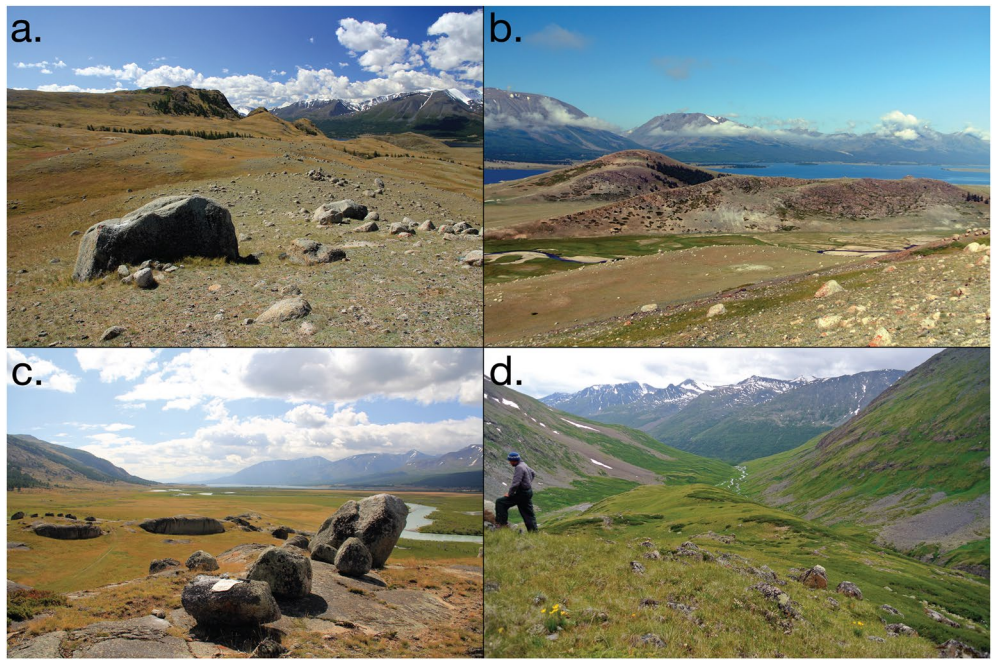

Figure 4. Photographs showing landforms discussed in the text. (a) Vantage south-southeast along Khoton Moraine II (48.691960°N, 88.363354°E). (b) Vantage from Biluut 3 south toward Khoton Nuur. In the foreground is Biluut 2 with Biluut 1 directly behind (48.654994°N, 88.351477°E). (c) Vantage southeast across Khoton Erratics II feature. Note the rounded, polished boulders resting directly upon ice-molded bedrock (48.743641°N, 88.164212°E). (d. Vantage from Takhilt Valley Moraine I southwest toward the Tsagaan-Sol Gol (48.971119°N, 88.080110°E).

We employed a combination of compass-clinometer to chart azimuthal elevations and bearings, respectively, of the surrounding skyline for determining topographic shielding corrections. We measured the strike and dip of each sampled surface using the GeoID™ application on a calibrated Apple iPad or else using a Brunton compass. Topographic shielding corrections were later calculated using the University of Washington (UW) online calcu-

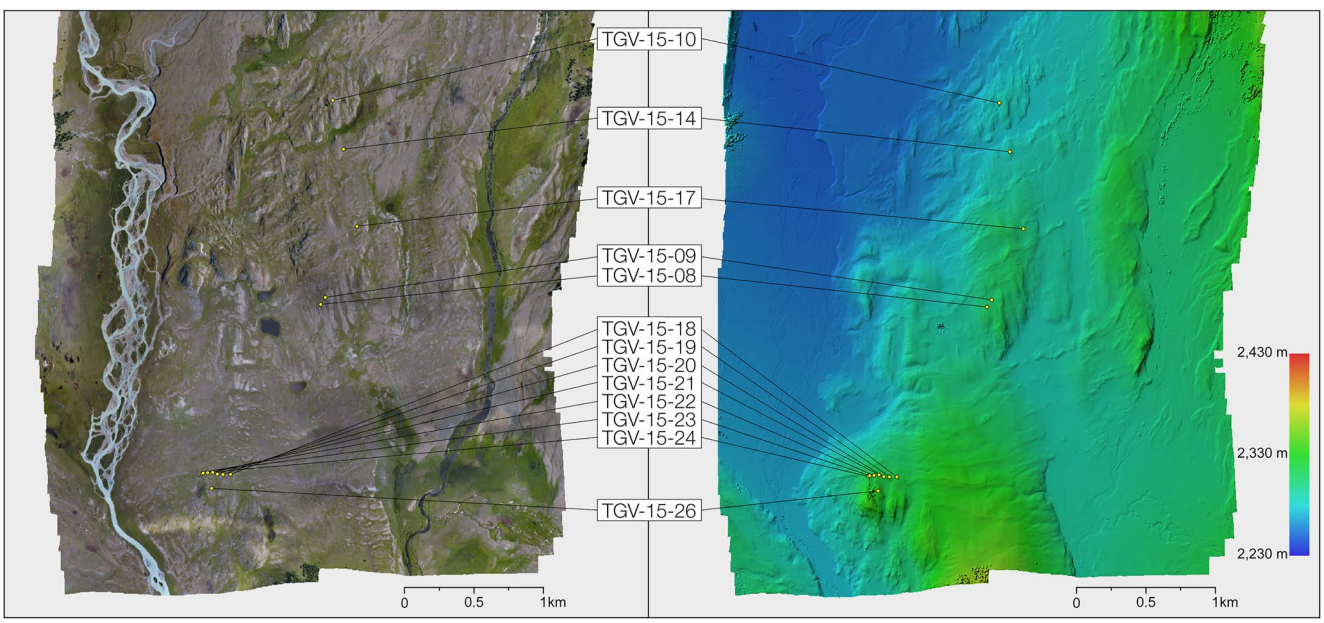

Figure 5. Tsagaan Sol landform elevation data and orthoimagery photogrammetrically derived from drone photographs. Left side shows ortho-mosaic (12.6 cm/px) and right side shows DEM (50.5 cm/px).

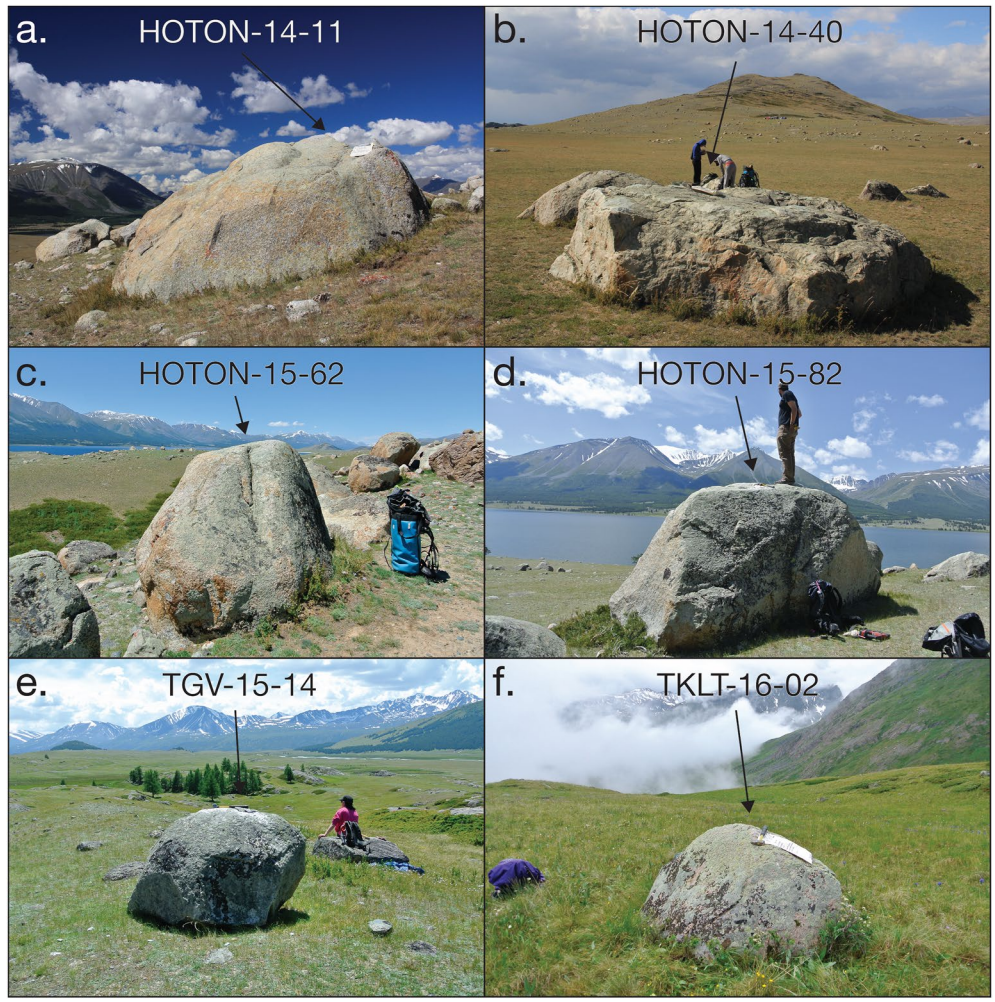

Figure 6. Examples of boulders sampled for ^{10}Be surface-exposure dating. (a) Photograph, with vantage northwest, of an ~2-m high boulder on Khoton Moraine II. (b) Photograph, vantage west-northwest, of an ~1-m high boulder selected for sampling at the base of Biluut 3. (c) Photograph, vantage north-northwest, of a large boulder rooted in Khoton Moraine I. (d) Photograph, vantage south, of a glacial erratic boulder resting on till-mantled bedrock near Khoton Nuur. Khoton Nuur is visible in the background. (e) Photograph, vantage north, of an ~1-m high glacial erratic boulder resting on till-mantled bedrock in the Tsagaan-Sol Valley. (f) Photograph, vantage southwest, of a boulder embedded in Takhilt Moraine I.

lator available at http://stoneage.ice-d.org/math/skyline/skyline_in.html. Each boulder was photographed from several vantages (some examples are shown in Figure 6) and also sketched in a notebook.

Samples were processed for ^{10}Be analysis at the University of Maine Glacial Geology and Geochronology Laboratory and also at the Lamont-Doherty Earth Observatory Cosmogenic Isotope Laboratory. We followed the laboratory protocols adapted from Schaefer et al. (2009) and Putnam et al. (2019), available online at https://umaine.edu/earthclimate/research/glacial-geology-and-geochronology-research-group/cosmogenicisotope/. Whole-rock samples were crushed to 125–710 μm grain-size fractions and boiled in H_3PO_4 and NaOH solutions. Quartz was separated from feldspar fractions using the froth flotation method described in Kawatra and Eisele (1992). Remaining quartz was subjected to several rounds of etching in 2% and 5% HF/HNO_3 solutions. We measured Al, Ca, Ti, Fe, and Be concentrations in the quartz using an Inductively Coupled Plasma Optical Emission Spectrometer (ICP-OES) to verify purity before moving forward with ion chromatography steps. Once pure, quartz samples were weighed, spiked with ~0.2 g of ^{9}Be carrier, and dissolved in concentrated HF. We used three ^{9}Be carriers in this study: LDEO carrier 5 (initial ^{9}Be concentration = 1,035 ppm), UMaine Phena 1A carrier (initial ^{9}Be concentration = 203 ppm), and VWR-Chemicals BDH Beryllium carrier (initial ^{9}Be concentration = 999 ppm). All beryllium carrier concentrations have been corrected for evaporation effects following Putnam et al. (2019)

Paleoceanography and Paleoclimatology

10.1029/2022PA004423

Table 1
^{10}Be Sample Details and Analytical Data

Landform name	Sample ID	CAMS laboratory number	Laboratory used	Latitude (DD)	Longitude (DD)	Elevation (m a.s.l.)	Boulder size (L × W × H) (cm)	Sample thickness (cm)	Density (g cm^{-2})	Shielding correction	Quartz weight (g)	Carrier added (g)	Carrier conc. (ppm)	^{10}Be/^{9}Be ± 1σ (10^{-14})	[^{10}Be] ± 1σ (10^{4}) (atoms/gram)	AMS std
Khoton Moraine IV	HOTON-14-22	BE45351	UMaine	48.700661408	88.380230566	2482.52	220 × 165 × 83	1.351	2.7	0.9948	10.4655	0.2075	994	52.02 ± 0.91	67.84 ± 1.19	07KNSTD
Khoton Moraine IV	HOTON-14-23	BE45352	UMaine	48.701751402	88.379322874	2485.78	175 × 120 × 68	1.129	2.7	0.9888	10.2968	0.2076	994	61.46 ± 1.09	81.64 ± 1.45	07KNSTD
Khoton Moraine IV	HOTON-14-24	BE45353	UMaine	48.705213609	88.375048093	2482.57	140 × 120 × 40	1.198	2.7	0.9970	10.2503	0.2077	994	73.39 ± 1.41	98.09 ± 1.89	07KNSTD
Khoton Moraine IV	HOTON-14-26	BE45354	UMaine	48.707101783	88.372131686	2480.45	300 × 230 × 47	1.612	2.7	0.9995	10.1617	0.2080	994	158.78 ± 3.83	215.14 ± 5.19	07KNSTD
Khoton Moraine IV	HOTON-14-28	BE45355	UMaine	48.707363104	88.370525818	2472.94	122 × 95 × 55	1.321	2.7	0.9991	10.2694	0.2067	994	72.92 ± 1.38	96.80 ± 1.84	07KNSTD
Khoton Moraine IV	HOTON-14-29	BE45356	UMaine	48.708838808	88.368647202	2473.64	225 × 195 × 63	0.824	2.7	0.9980	10.4070	0.2070	994	196.48 ± 2.78	258.87 ± 3.67	07KNSTD
Khoton Moraine IV	HOTON-14-31	BE45357	UMaine	48.715739670	88.353812508	2483.89	220 × 150 × 103	1.212	2.7	0.9771	10.4384	0.2073	994	74.39 ± 1.49	97.46 ± 1.95	07KNSTD
Khoton Moraine III	HOTON-14-33	BE45416	UMaine	48.710827844	88.353851099	2462.97	280 × 225 × 54	1.675	2.7	0.9995	9.0139	0.2056	996	67.87 ± 1.60	102.17 ± 2.40	07KNSTD
Khoton Moraine III	HOTON-14-34	BE45417	UMaine	48.705357688	88.369818719	2460.63	367 × 288 × 85	1.293	2.7	0.9999	8.2595	0.2051	996	38.95 ± 0.51	63.44 ± 0.84	07KNSTD
Khoton Moraine III	HOTON-14-35	BE45418	UMaine	48.701765203	88.372890801	2454.77	197 × 180 × 57	1.012	2.7	0.9984	8.0132	0.2052	996	36.90 ± 0.69	61.93 ± 1.16	07KNSTD
Khoton Moraine III	HOTON-14-36	BE45419	UMaine	48.699841365	88.374645308	2452.30	295 × 245 × 42	1.392	2.7	0.9964	10.5586	0.2051	996	51.57 ± 0.96	65.95 ± 1.23	07KNSTD
Khoton Moraine III	HOTON-14-37	BE45420	UMaine	48.699711674	88.374489973	2453.19	276 × 245 × 33	1.120	2.7	0.9995	7.3752	0.2050	996	34.70 ± 0.65	63.15 ± 1.18	07KNSTD
Khoton Moraine III	HOTON-15-104	BE45669	UMaine	48.699540657	88.369724316	2432.32	232 × 179 × 51	1.112	2.7	0.9999	2.6859	0.2039	998	11.98 ± 0.32	57.91 ± 1.59	07KNSTD
Khoton Moraine III	HOTON-15-105	BE45670	UMaine	48.699696340	88.369583104	2432.72	257 × 192 × 88	1.219	2.7	0.9999	7.2543	0.2046	998	33.71 ± 0.63	62.38 ± 1.17	07KNSTD
Khoton Moraine III	HOTON-15-106	BE45671	UMaine	48.700097413	88.368895495	2432.13	148 × 112 × 57	0.728	2.7	0.9985	4.9140	0.2050	998	36.24 ± 0.68	99.32 ± 1.86	07KNSTD
Khoton Moraine III	HOTON-15-109	BE45672	UMaine	48.704967548	88.362318317	2443.76	182 × 123 × 48	1.403	2.7	0.9976	9.8746	0.2038	998	52.24 ± 0.99	71.14 ± 1.35	07KNSTD
Khoton Moraine II	HOTON-14-08	BE40283	UMaine	48.681834180	88.367138898	2330.69	255 × 180 × 59	1.630	2.7	0.9901	5.4842	0.2014	1,037	20.37 ± 0.54	51.75 ± 1.37	07KNSTD
Khoton Moraine II	HOTON-14-09	BE40284	UMaine	48.682589157	88.367694531	2334.76	345 × 230 × 96	1.550	2.7	0.9797	5.4886	0.2036	1,037	20.22 ± 0.37	51.91 ± 0.96	07KNSTD
Khoton Moraine II	HOTON-14-10	BE40941	UMaine	48.683062811	88.368107370	2332.87	260 × 250 × 61	1.420	2.7	0.9855	5.2603	0.1831	1,037	21.53 ± 0.41	51.35 ± 1.02	07KNSTD
Khoton Moraine II	HOTON-14-11	BE40286	UMaine	48.685526903	88.367851662	2340.99	420 × 315 × 128	1.710	2.7	0.9993	5.9027	0.1831	1,037	23.53 ± 0.39	50.07 ± 0.87	07KNSTD

Paleoceanography and Paleoclimatology

10.1029/2022PA004423

Table 1
Continued

Landform name	Sample ID	CAMS laboratory number	Laboratory used	Latitude (DD)	Longitude (DD)	Elevation (m a.s.l.)	Boulder size (L × W × H) (cm)	Sample thickness (cm)	Density (g cm^{-2})	Shielding correction	Quartz weight (g)	Carrier added (g)	Carrier conc. (ppm)	$^{10}Be/^{9}Be \pm 1\sigma$ (10^{-14})	$[^{10}Be] \pm 1\sigma$ (10^{4}) (atoms/gram)	AMS std
Khoton Moraine II	HOTON-14-12	BE40287	UMaine	48.686424310	88.367536494	2343.14	205 × 185 × 94	1.210	2.7	0.9984	5.5288	0.2026	1,037	21.09 ± 0.44	53.46 ± 1.12	07KNSTD
Khoton Moraine II	HOTON-14-13	BE40288	UMaine	48.687260251	88.366418533	2345.60	170 × 130 × 78	1.870	2.7	0.9916	7.5267	0.2021	1,037	29.18 ± 0.54	54.22 ± 1.00	07KNSTD
Khoton Moraine II	HOTON-14-15	BE40943	UMaine	48.690857314	88.364314878	2353.15	270 × 220 × 40	1.550	2.7	0.9993	5.6724	0.1826	1,037	23.19 ± 0.44	51.21 ± 1.01	07KNSTD
Khoton Moraine II	HOTON-14-18	BE40944	UMaine	48.692843884	88.359866696	2353.56	220 × 200 × 80	0.880	2.7	0.9987	3.5135	0.1817	1,037	17.85 ± 0.34	63.12 ± 1.28	07KNSTD
Khoton Moraine I	HOTON-15-58	BE43557	UMaine	48.613232171	88.430928330	2117.51	125 × 100 × 61	1.136	2.7	0.9955	15.9855	0.2062	981	49.43 ± 1.06	41.33 ± 0.89	07KNSTD
Khoton Moraine I	HOTON-15-62	BE43558	UMaine	48.617094763	88.426908898	2117.98	260 × 235 × 156	1.064	2.7	0.9963	16.2424	0.2056	981	51.63 ± 0.98	42.38 ± 0.80	07KNSTD
Khoton Moraine I	HOTON-15-63	BE43559	UMaine	48.617203369	88.426771643	2118.39	270 × 220 × 105	1.381	2.7	0.9966	16.4008	0.2021	981	53.06 ± 1.00	42.41 ± 0.80	07KNSTD
Khoton Biluuts	HOTON-14-01	BE39009	LDEO	48.651683389	88.354324533	2182.74	110 × 110 × 59	0.980	2.7	0.9996	5.0291	0.1809	1,035	18.01 ± 0.29	44.74 ± 0.73	07KNSTD
Khoton Biluuts	HOTON-14-02	BE39010	LDEO	48.651642567	88.354371576	2182.85	140 × 95 × 55	0.960	2.7	0.9997	5.0227	0.1805	1,035	17.45 ± 0.28	43.31 ± 0.71	07KNSTD
Khoton Biluuts	HOTON-14-03	BE39011	LDEO	48.651243210	88.354275411	2175.55	105 × 105 × 51	0.960	2.7	0.9720	5.0226	0.1804	1,035	18.18 ± 0.30	45.09 ± 0.73	07KNSTD
Khoton Biluuts	HOTON-14-04	BE39012	LDEO	48.650402551	88.355177435	2158.58	185 × 155 × 78	1.160	2.7	0.9985	5.0071	0.1806	1,035	16.87 ± 0.32	42.01 ± 0.79	07KNSTD
Khoton Biluuts	HOTON-14-20	BE40947	UMaine	48.655151384	88.350596918	2254.05	110 × 70 × 49	1.060	2.7	0.9996	5.4180	0.1815	1,037	19.65 ± 0.41	45.04 ± 0.99	07KNSTD
Khoton Biluuts	HOTON-14-21	BE40948	UMaine	48.655673067	88.350425832	2259.81	265 × 205 × 85	2.040	2.7	0.9946	5.2561	0.1797	1,037	19.61 ± 0.49	45.90 ± 1.18	07KNSTD
Khoton Biluuts	HOTON-14-38	BE39013	LDEO	48.647849378	88.358911962	2113.63	390 × 277 × 89	0.970	2.7	0.9996	5.0202	0.1806	1,035	16.97 ± 0.29	42.15 ± 0.72	07KNSTD
Khoton Biluuts	HOTON-14-40	BE39014	LDEO	48.645441782	88.360574205	2105.90	350 × 347 × 96	1.750	2.7	0.9998	5.0374	0.1808	1,035	16.43 ± 0.27	40.71 ± 0.66	07KNSTD
Khoton Biluuts	HOTON-15-95	BE41958	UMaine	48.651495931	88.325624781	2186.95	204 × 190 × 63	0.554	2.7	0.9937	10.3283	0.1844	1,037	35.81 ± 0.76	44.17 ± 0.93	07KNSTD
Khoton Erratics I	HOTON-15-80	BE43930	UMaine	48.646225231	88.324094259	2105.20	445 × 370 × 161	0.618	2.7	0.9853	17.1558	1.0077	203	50.28 ± 1.35	39.95 ± 1.07	07KNSTD
Khoton Erratics I	HOTON-15-81	BE43931	UMaine	48.646522187	88.323519041	2107.96	613 × 531 × 175	0.802	2.7	0.9933	16.9299	1.0092	203	49.58 ± 0.93	39.97 ± 0.75	07KNSTD
Khoton Erratics I	HOTON-15-82	BE43932	UMaine	48.647172283	88.322678305	2119.16	650 × 617 × 240	1.137	2.7	0.9981	19.8344	1.0116	203	59.37 ± 0.97	40.98 ± 0.67	07KNSTD
Khoton Erratics II	HOTON-14-42	BE43552	UMaine	48.743686484	88.163773419	2123.00	170 × 130 x 75	0.950	2.7	0.9935	16.5246	0.2048	981	47.42 ± 0.77	38.09 ± 0.62	07KNSTD

Paleoceanography and Paleoclimatology

10.1029/2022PA004423

Table 1
Continued

Landform name	Sample ID	CAMS laboratory number	Laboratory used	Latitude (DD)	Longitude (DD)	Elevation (m a.s.l.)	Boulder size (L × W × H) (cm)	Sample thickness (cm)	Density (g cm^{-2})	Shielding correction	Quartz weight (g)	Carrier added (g)	Carrier conc. (ppm)	$^{10}Be/^{9}Be \pm 1\sigma$ (10^{-14})	[^{10}Be] ± 1σ (10^{4}) (atoms/gram)	AMS std
Khoton Erratics II	HOTON-14-43	BE43553	UMaine	48.743642372	88.163832631	2122.88	110 × 80 × 56	1.280	2.7	0.9980	3.1690	0.2045	981	9.93 ± 0.17	39.66 ± 0.72	07KNSTD
Khoton Erratics II	HOTON-14-44	BE43554	UMaine	48.743549713	88.163738509	2121.50	150 × 77 × 43	1.880	2.7	0.9986	14.3014	0.2071	981	40.60 ± 0.98	38.02 ± 0.92	07KNSTD
Khoton Erratics II	HOTON-14-46	BE43555	UMaine	48.743320000	88.164724268	2116.11	170 × 163 × 46	2.470	2.7	0.9970	17.1636	0.2072	981	50.94 ± 0.96	39.88 ± 0.75	07KNSTD
Khoton Erratics II	HOTON-14-47	BE43556	UMaine	48.743533807	88.164845436	2116.75	73 × 40 × 43	1.630	2.7	0.9988	6.7836	0.2066	981	20.21 ± 0.33	39.25 ± 0.65	07KNSTD
Tsagaan-Sol Moraine I	TGV-15-18	BE41783	UMaine	48.793568383	88.129471705	2175.50	275 × 182 × 109	1.390	2.7	0.9990	8.2221	0.1853	1,037	28.21 ± 0.53	43.90 ± 0.82	07KNSTD
Tsagaan-Sol Moraine I	TGV-15-19	BE41784	UMaine	48.793383894	88.128280556	2168.13	403 × 273 × 132	1.079	2.7	0.9887	8.2432	0.1842	1,037	25.26 ± 0.47	38.95 ± 0.73	07KNSTD
Tsagaan-Sol Moraine I	TGV-15-20	BE41785	UMaine	48.793399154	88.125715155	2159.52	346 × 243 × 116	0.926	2.7	0.9953	8.0190	0.1847	1,037	45.24 ± 0.99	72.05 ± 1.57	07KNSTD
Tsagaan-Sol Moraine I	TGV-15-21	BE41786	UMaine	48.793693045	88.124583105	2158.08	282 × 275 × 61	1.214	2.7	0.9990	8.1687	0.1847	1,037	20.68 ± 0.47	32.25 ± 0.73	07KNSTD
Tsagaan-Sol Moraine I	TGV-15-22	BE41787	UMaine	48.793803324	88.123924126	2158.90	373 × 215 × 125	1.296	2.7	0.9995	8.1151	0.1851	1,037	39.30 ± 0.67	61.95 ± 1.06	07KNSTD
Tsagaan-Sol Moraine I	TGV-15-23	BE41788	UMaine	48.793739596	88.123527839	2160.11	566 × 363 × 359	0.888	2.7	0.9965	8.1631	0.1850	1,037	25.54 ± 0.53	39.95 ± 0.83	07KNSTD
Tsagaan-Sol Moraine I	TGV-15-24	BE41789	UMaine	48.793740656	88.123527842	2160.14	776 × 497 × 256	1.159	2.7	0.9983	8.3945	0.1841	1,037	63.95 ± 0.95	97.06 ± 1.44	07KNSTD
Tsagaan-Sol Erratics	TGV-15-08	BE45572	UMaine	48.811245516	88.132560731	2138.05	280 × 183 × 131	0.413	2.7	0.9996	10.9914	0.2055	997	29.67 ± 0.64	36.17 ± 0.78	07KNSTD
Tsagaan-Sol Erratics	TGV-15-09	BE45573	UMaine	48.811507723	88.132319826	2137.83	340 × 309 × 102	0.459	2.7	0.9998	10.1302	0.2048	997	27.80 ± 0.52	36.59 ± 0.69	07KNSTD
Tsagaan-Sol Erratics	TGV-15-10	BE45574	UMaine	48.830322328	88.131886121	2134.39	713 × 354 × 321	0.797	2.7	0.9972	10.2894	0.2043	997	29.26 ± 0.54	37.87 ± 0.71	07KNSTD
Tsagaan-Sol Erratics	TGV-15-14	BE45575	UMaine	48.823420286	88.133712197	2152.97	160 × 133 × 102	1.319	2.7	0.9989	10.7002	0.2048	997	29.70 ± 0.48	37.06 ± 0.60	07KNSTD
Tsagaan-Sol Erratics	TGV-15-17	BE45576	UMaine	48.816023002	88.136162554	2152.05	215 × 146 × 92	1.496	2.7	0.9984	10.3960	0.2040	997	28.84 ± 0.46	36.87 ± 0.60	07KNSTD
Tsagaan-Sol Erratics	TGV-15-26	BE45577	UMaine	48.793046135	88.123578758	2165.07	204 × 180 × 112	1.123	2.7	0.9994	10.9528	0.2041	997	33.53 ± 0.62	40.83 ± 0.76	07KNSTD

Table 1
Continued

Landform name	Sample ID	CAMS laboratory number	Laboratory used	Latitude (DD)	Longitude (DD)	Elevation (m a.s.l.)	Boulder size (L × W × H) (cm)	Sample thickness (cm)	Density (g cm^{-2})	Shielding correction	Quartz weight (g)	Carrier added (g)	Carrier conc. (ppm)	^{10}Be/^{9}Be ± 1σ (10^{-14})	[^{10}Be] ± 1σ (10^{4}) (atoms/gram)	AMS std
Takhilt Valley Moraine I	TKLT-16-02	BE45568	UMaine	48.969240675	88.078976837	2681.35	220 × 155 × 101	3.157	2.7	0.9889	2.8862	0.2053	997	11.35 ± 0.21	50.80 ± 0.98	07KNSTD
Takhilt Valley Moraine I	TKLT-16-05	BE45569	UMaine	48.971588511	88.080177385	2728.50	136 × 116 × 87	1.324	2.7	0.9906	3.8434	0.2052	997	14.97 ± 0.31	50.99 ± 1.06	07KNSTD
Takhilt Valley Moraine I	TKLT-16-07	BE45570	UMaine	48.972330472	88.081185382	2762.69	180 × 100 × 96	2.142	2.7	0.9907	10.9181	0.2043	997	44.02 ± 0.82	54.09 ± 1.01	07KNSTD

and are reported in Table 2. Samples were subjected to chromatography techniques to isolate the Beryllium fraction following the methods of Schaefer et al. (2009) and references therein. BeOH samples were then precipitated, oxidized to BeO by combusting at 900°C for 90 min, and finally mixed with small amounts of niobium and packed into cathodes for Be analyses. All ^{10}Be/^{9}Be measurements were conducted at the Lawrence-Livermore National Laboratory Center for Accelerator Mass Spectrometry (LLNL-CAMS). Sample ratios were measured relative to the 07KNSTD standard (^{10}Be/^{9}Be = 2.85e^{-12}; Nishiizumi et al., 2007). Measurements were then corrected for boron contamination and for ^{10}Be in procedural blanks. Reported sample ^{10}Be concentration uncertainties have been propagated with uncertainties attending measured blank ^{10}Be concentrations (Table 2). Analytical uncertainties are generally ~2%.

^{10}Be surface-exposure age calculations were carried out using Version 3 of the online UW cosmogenic calculators (Balco, 2017; Balco et al., 2008, 2011). Full documentation of Version 3 calculator is available online at https://sites.google.com/a/bgc.org/v3docs/. We calculated ages using the ^{10}Be production rate calibration data set determined from the Rannoch Moor calibration site, central Scottish Highlands, reported by Putnam et al. (2019). We chose this production rate calibration data set because it is based on an independently ^{14}C-dated set of glacial landforms that are located at a similar latitude in the Northern Hemisphere to our Mongolian field sites. Our approach is similar to that of Lifton, Beel, et al. (2014), who used the northeastern North American calibration data set (Balco et al., 2009) to calculate a ^{10}Be chronology for moraines in the nearby Kyrgyz Tien Shan. We also present ages calculated using a modified version of the "Primary" global calibration data set of Borchers et al. (2016), in which we substituted previous Scotland data with the more recent, radiocarbon-constrained calibration data set of Putnam et al. (2019) (Table 3). We calculated ages with the time-independent scaling method of Lal (1991) and Stone (2000) ("St"), a time-dependent scaling version of Lal (1991) and Stone (2000) that incorporates a high-resolution geomagnetic model of Lifton, Sato and Dunai (2014) and Lifton et al. (2016); "Lm"), and the time-dependent, nuclide-dependent, scaling model of Lifton, Sato and Dunai (2014) ("LSDn"). We assumed a rock density of 2.7 g/cm^3 and applied thickness corrections for each sample. Erosion rates were not incorporated into the age calculations because the presence of glacial polish, striations, and rock varnish indicates that surface erosion has been negligible for boulder surfaces selected for sampling. Wintertime satellite imagery from the region indicates that boulder tops and moraine ridges remain exposed and free of snow throughout the winter season likely due to low snow accumulation rates and wind. Therefore, we did not apply any corrections for snow cover.

7. Results

Of 187 samples collected in the field, we processed 60 samples for ^{10}Be analyses. Analytical results and procedural blank data are given in Tables 1 and 2, respectively. We note that our use of two laboratories and multiple low-level background beryllium carriers across multiple years produces consistent ^{10}Be/^{9}Be ratios from multiple samples from the same landforms (see Table 1 for details). Exposure ages are reported in Table 3 and shown on the map in Figure 7. Input data formatted for exposure-age calculations using Version 3 of the online University of Washington cosmogenic exposure-age calculators are included in Tables S1–S3 in Supporting Information S1. Hereafter, we discuss ages calculated using the Putnam et al. (2019) calibration data set and the "St" scaling protocol of Lal (1991) and Stone (2000). We prefer ages calculated using this scaling model (Lal, 1991; Stone, 2000) because it affords good agreement among sea-level high-latitude "reference" production rates determined from independently dated calibration landforms at a variety of different latitudes and altitudes (Putnam et al., 2019). However, we note that other production rates and scaling models produce similar exposure ages and thus, our conclusions do not depend strongly on a choice of calibration data set or the scaling model. Eventual development of a regional calibration data set from Central Asia would aid in reducing scaling uncertainties and in refining the accuracy of ^{10}Be chronologies generated from this area.

Table 2
^{10}Be Procedural Blank Data

Blank no.	CAMS laboratory no.	Sample ID	Corresponding samples	Be carrier name	Carrier added (g)	Carrier conc. (ppm)	^{10}Be/^{9}Be ± 1σ (10^{-16})	N[^{10}Be] ± 1σ (10^{3} atoms)	Average ^{9}Be current (μA) (runs)	AMS std
1	BE39002	BLK1-2015Apr21	HOTON-14-01, 02, 03, 04, 38, 40	LDEO carrier 5	0.1807	1,035	2.98 ± 0.88	3.72 ± 1.09	28.8 (2)	07KNSTD
2	BE40289	B15a-2015Dec17	HOTON-14-08, 09, 12	LDEO carrier 5	0.2032	1,037	2.80 ± 2.56	3.94 ± 3.61	29.8 (2)	07KNSTD
3	BE40290	B15b-2015Dec17	HOTON-14-13	LDEO carrier 5	0.2019	1,037	4.24 ± 1.58	5.93 ± 2.21	22.7 (2)	07KNSTD
4	BE40946	B19-2016Apr15	HOTON-14-10, 11, 15, 18, 20, 21	LDEO carrier 5	0.1817	1,038	25.73 ± 0.12	32.42 ± 15.12	22.6 (2)	07KNSTD
5	BE41790	B25-2016Sept2	TGV-15-18, 19, 20, 21, 22, 23, 24	LDEO carrier 5	0.1838	1,037	9.87 ± 1.67	12.57 ± 2.13	25.8 (2)	07KNSTD
6	BE41954	B27-2016Oct21	HOTON-15-95	LDEO carrier 5	0.1852	1,037	11.12 ± 1.86	14.38 ± 2.13	24.7 (2)	07KNSTD
7	BE43560	B50-2017Sept7	HOTON-14-42, 43, 44, 46, 47, 58, 62, 63	VWR-Chemicals BDH carrier	0.2063	981	54.47 ± 1.87	73.97 ± 6.21	21.2 (2)	07KNSTD
8	BE43937	B57-2017Dec8	HOTON-15-80, 81, 82	UMaine Phena 1A carrier	1.0106	203	14.45 ± 3.41	19.99 ± 4.68	19.8 (2)	07KNSTD
9	BE45350	B62-2018Sept9	HOTON-14-22, 23, 24, 26, 28, 29, 31	VWR-Chemicals BDH carrier	0.2079	994	50.01 ± 4.20	69.04 ± 5.80	23.0 (2)	07KNSTD
10	BE45415	B65-2018Oct5	HOTON-14-33, 34, 35, 36, 37	VWR-Chemicals BDH carrier	0.2046	996	55.59 ± 4.73	76.07 ± 6.45	21.0 (2)	07KNSTD
11	BE45571	B68-2018Oct25	TKLT-16-02, 05, 07; TGV-15-08, 09, 10, 14, 17, 26	VWR-Chemicals BDH carrier	0.2051	997	63.27 ± 5.01	86.43 ± 6.84	21.6 (2)	07KNSTD
12	BE45673	B70a-2018Nov2	HOTON-15-104, 105, 106, 109	VWR-Chemicals BDH carrier	0.2044	998	54.37 ± 4.91	74.117 ± 6.69	18.0 (2)	07KNSTD

Individual exposure ages are reported with 1σ analytical uncertainties. Landform ages are reported as the arithmetic mean along with both the standard error of the mean and an "external uncertainty," stated in parentheses, that includes the standard error propagated in quadrature with the production-rate uncertainty. For each landform population, we excluded exposure ages that were either morphostratigraphically discordant or samples that deviated significantly from the moraine age population (i.e., as determined using Peirce's criterion or chi-square statistics). A detailed report for each sample population can be found in Text S1 in Supporting Information S1, and additional statistics for exposure age populations are provided in Table 4. All ages are reported to one digit beyond the significant figure, following the convention set forth by Stuiver and Polach (1977).

Exposure ages from the Khoton Nuur moraines and inboard landforms exhibit generally good internal consistency and most form approximately normal distributions (Figure 8). The outermost moraine of the Khoton Nuur belt (Khoton IV) yields a mean landform age of 35,440 ± 210 (980) years (n = 7, −4 outliers). Inboard moraine ridges afford ages of 23,430 ± 570 (850) years (Khoton III; n = 9, −2 outliers), 20,780 ± 230 (610) years (Khoton II; n = 8, −1 outlier), and 19,520 ± 160 (550) years (Khoton I; n = 3). A cluster of glacial erratic boulders located on the Khoton Biluuts, just inboard of the Khoton I belt, date to 19,250 ± 110 (530) years (n = 9, −1 outlier;

Table 3
^{10}Be Surface-Exposure Ages (in Thousands of Years Before AD 2015; ±1σ)

			Rannoch Moor, Scotland rate of Putnam et al. (2019)			"Primary" global rate of Borchers et al. (2016): Scotland sites replaced with Putnam et al. (2019)		
Landform	Sample ID	Nuclide	St age (ka)	Lm age (ka)	LSDn age (ka)	St age (ka)	Lm age (ka)	LSDn age (ka)
Khoton Moraine IV	HOTON-14-22 *	Be-10 (qtz)	**24.49 ± 0.43**	24.63 ± 0.44	23.63 ± 0.42	23.93 ± 0.42	23.44 ± 0.41	22.17 ± 0.39
Khoton Moraine IV	HOTON-14-23 *	Be-10 (qtz)	**29.57 ± 0.53**	29.55 ± 0.53	28.30 ± 0.51	28.89 ± 0.52	28.11 ± 0.50	26.52 ± 0.48
Khoton Moraine IV	HOTON-14-24	Be-10 (qtz)	**35.38 ± 0.69**	35.33 ± 0.69	33.84 ± 0.66	34.57 ± 0.67	33.60 ± 0.65	31.59 ± 0.61
Khoton Moraine IV	HOTON-14-26 *	Be-10 (qtz)	**78.64 ± 1.94**	78.10 ± 1.92	74.62 ± 1.84	76.81 ± 1.89	74.18 ± 1.82	69.73 ± 1.71
Khoton Moraine IV	HOTON-14-28	Be-10 (qtz)	**35.11 ± 0.67**	35.06 ± 0.67	33.60 ± 0.64	34.30 ± 0.66	33.33 ± 0.64	31.36 ± 0.60
Khoton Moraine IV	HOTON-14-29 *	Be-10 (qtz)	**94.95 ± 1.38**	93.98 ± 1.36	89.87 ± 1.30	92.73 ± 1.35	89.29 ± 1.29	84.06 ± 1.22
Khoton Moraine IV	HOTON-14-31	Be-10 (qtz)	**35.84 ± 0.72**	35.78 ± 0.72	34.26 ± 0.69	35.01 ± 0.71	34.03 ± 0.69	32.00 ± 0.65
Khoton Moraine III	HOTON-14-33 *	Be-10 (qtz)	**37.42 ± 0.89**	37.33 ± 0.89	35.76 ± 0.85	36.56 ± 0.87	35.48 ± 0.84	33.50 ± 0.80
Khoton Moraine III	HOTON-14-34	Be-10 (qtz)	**23.11 ± 0.31**	23.29 ± 0.31	22.38 ± 0.30	22.58 ± 0.30	22.17 ± 0.30	21.03 ± 0.28
Khoton Moraine III	HOTON-14-35	Be-10 (qtz)	**22.63 ± 0.43**	22.82 ± 0.43	21.95 ± 0.41	22.11 ± 0.42	21.73 ± 0.41	20.62 ± 0.39
Khoton Moraine III	HOTON-14-36	Be-10 (qtz)	**24.28 ± 0.46**	24.42 ± 0.46	23.47 ± 0.44	23.72 ± 0.45	23.23 ± 0.44	22.02 ± 0.41
Khoton Moraine III	HOTON-14-37	Be-10 (qtz)	**23.10 ± 0.44**	23.28 ± 0.44	22.38 ± 0.42	22.57 ± 0.43	22.15 ± 0.42	21.03 ± 0.40
Khoton Moraine III	HOTON-15-104	Be-10 (qtz)	**21.47 ± 0.59**	21.70 ± 0.60	20.92 ± 0.58	20.97 ± 0.58	20.67 ± 0.57	19.65 ± 0.54
Khoton Moraine III	HOTON-15-105	Be-10 (qtz)	**23.15 ± 0.44**	23.32 ± 0.44	22.45 ± 0.42	22.61 ± 0.43	22.20 ± 0.42	21.09 ± 0.40
Khoton Moraine III	HOTON-15-106 *	Be-10 (qtz)	**36.89 ± 0.70**	36.81 ± 0.70	35.31 ± 0.67	36.04 ± 0.68	34.98 ± 0.66	33.07 ± 0.62
Khoton Moraine III	HOTON-15-109	Be-10 (qtz)	**26.32 ± 0.50**	26.39 ± 0.50	25.35 ± 0.48	25.71 ± 0.49	25.11 ± 0.48	23.79 ± 0.45
Khoton Moraine II	HOTON-14-08	Be-10 (qtz)	**20.87 ± 0.56**	21.12 ± 0.56	20.48 ± 0.55	20.39 ± 0.54	20.11 ± 0.54	19.22 ± 0.51
Khoton Moraine II	HOTON-14-09	Be-10 (qtz)	**21.08 ± 0.39**	21.33 ± 0.40	20.67 ± 0.39	20.59 ± 0.38	20.30 ± 0.38	19.40 ± 0.36
Khoton Moraine II	HOTON-14-10	Be-10 (qtz)	**20.73 ± 0.42**	21.00 ± 0.42	20.35 ± 0.41	20.26 ± 0.41	19.99 ± 0.40	19.11 ± 0.38
Khoton Moraine II	HOTON-14-11	Be-10 (qtz)	**19.87 ± 0.35**	20.16 ± 0.35	19.54 ± 0.34	19.41 ± 0.34	19.19 ± 0.33	18.34 ± 0.32
Khoton Moraine II	HOTON-14-12	Be-10 (qtz)	**21.12 ± 0.45**	21.37 ± 0.45	20.70 ± 0.44	20.64 ± 0.44	20.35 ± 0.43	19.43 ± 0.41
Khoton Moraine II	HOTON-14-13	Be-10 (qtz)	**21.65 ± 0.40**	21.88 ± 0.41	21.18 ± 0.39	21.15 ± 0.39	20.83 ± 0.39	19.89 ± 0.37
Khoton Moraine II	HOTON-14-15	Be-10 (qtz)	**20.12 ± 0.40**	20.41 ± 0.41	19.76 ± 0.39	19.66 ± 0.39	19.43 ± 0.39	18.55 ± 0.37
Khoton Moraine II	HOTON-14-18 *	Be-10 (qtz)	**24.70 ± 0.50**	24.83 ± 0.51	23.98 ± 0.49	24.13 ± 0.49	23.62 ± 0.48	22.50 ± 0.46
Khoton Moraine I	HOTON-15-58	Be-10 (qtz)	**19.20 ± 0.41**	19.49 ± 0.42	19.11 ± 0.41	18.76 ± 0.41	18.56 ± 0.40	17.94 ± 0.39
Khoton Moraine I	HOTON-15-62	Be-10 (qtz)	**19.65 ± 0.37**	19.94 ± 0.38	19.54 ± 0.37	19.20 ± 0.37	18.98 ± 0.36	18.34 ± 0.35
Khoton Moraine I	HOTON-15-63	Be-10 (qtz)	**19.70 ± 0.37**	19.99 ± 0.38	19.59 ± 0.37	19.25 ± 0.37	19.03 ± 0.36	18.39 ± 0.35
Khoton Biluuts	HOTON-14-01	Be-10 (qtz)	**19.72 ± 0.32**	20.01 ± 0.33	19.55 ± 0.32	19.26 ± 0.32	19.04 ± 0.31	18.35 ± 0.30
Khoton Biluuts	HOTON-14-02	Be-10 (qtz)	**19.08 ± 0.31**	19.38 ± 0.32	18.94 ± 0.31	18.64 ± 0.31	18.45 ± 0.30	17.78 ± 0.29
Khoton Biluuts	HOTON-14-03 *	Be-10 (qtz)	**20.53 ± 0.34**	20.80 ± 0.34	20.32 ± 0.33	20.06 ± 0.33	19.80 ± 0.32	19.07 ± 0.31
Khoton Biluuts	HOTON-14-04	Be-10 (qtz)	**18.88 ± 0.36**	19.19 ± 0.36	18.78 ± 0.36	18.45 ± 0.35	18.27 ± 0.35	17.63 ± 0.33
Khoton Biluuts	HOTON-14-20	Be-10 (qtz)	**18.89 ± 0.42**	19.20 ± 0.42	18.70 ± 0.41	18.45 ± 0.41	18.28 ± 0.40	17.55 ± 0.39
Khoton Biluuts	HOTON-14-21	Be-10 (qtz)	**19.43 ± 0.50**	19.73 ± 0.51	19.20 ± 0.50	18.98 ± 0.49	18.78 ± 0.48	18.02 ± 0.47
Khoton Biluuts	HOTON-14-38	Be-10 (qtz)	**19.51 ± 0.33**	19.80 ± 0.34	19.42 ± 0.33	19.06 ± 0.33	18.85 ± 0.32	18.22 ± 0.31
Khoton Biluuts	HOTON-14-40	Be-10 (qtz)	**19.06 ± 0.31**	19.37 ± 0.32	19.00 ± 0.31	18.63 ± 0.31	18.44 ± 0.30	17.83 ± 0.29
Khoton Biluuts	HOTON-15-95	Be-10 (qtz)	**19.45 ± 0.41**	19.75 ± 0.42	19.29 ± 0.41	19.00 ± 0.40	18.80 ± 0.40	18.11 ± 0.38
Khoton Erratics I	HOTON-15-80	Be-10 (qtz)	**18.81 ± 0.51**	19.12 ± 0.51	18.76 ± 0.50	18.38 ± 0.49	18.20 ± 0.49	17.61 ± 0.47
Khoton Erratics I	HOTON-15-81	Be-10 (qtz)	**18.66 ± 0.35**	18.98 ± 0.36	18.62 ± 0.35	18.24 ± 0.35	18.07 ± 0.34	17.47 ± 0.33
Khoton Erratics I	HOTON-15-82	Be-10 (qtz)	**18.94 ± 0.31**	19.25 ± 0.32	18.87 ± 0.31	18.51 ± 0.30	18.33 ± 0.30	17.71 ± 0.29
Khoton Erratics II	HOTON-14-42	Be-10 (qtz)	**17.57 ± 0.29**	17.93 ± 0.29	17.57 ± 0.29	17.17 ± 0.28	17.06 ± 0.28	16.49 ± 0.27
Khoton Erratics II	HOTON-14-43	Be-10 (qtz)	**18.27 ± 0.33**	18.61 ± 0.34	18.23 ± 0.33	17.85 ± 0.33	17.71 ± 0.32	17.11 ± 0.31

Table 3
Continued

Landform	Sample ID	Nuclide	Rannoch Moor, Scotland rate of Putnam et al. (2019)			"Primary" global rate of Borchers et al. (2016): Scotland sites replaced with Putnam et al. (2019)		
			St age (ka)	Lm age (ka)	LSDn age (ka)	St age (ka)	Lm age (ka)	LSDn age (ka)
Khoton Erratics II	HOTON-14-44	Be-10 (qtz)	**17.61 ± 0.43**	17.96 ± 0.44	17.61 ± 0.43	17.21 ± 0.42	17.10 ± 0.42	16.52 ± 0.40
Khoton Erratics II	HOTON-14-46	Be-10 (qtz)	**18.67 ± 0.35**	18.99 ± 0.36	18.62 ± 0.35	18.24 ± 0.35	18.08 ± 0.34	17.47 ± 0.33
Khoton Erratics II	HOTON-14-47	Be-10 (qtz)	**18.20 ± 0.30**	18.54 ± 0.31	18.17 ± 0.30	17.78 ± 0.29	17.65 ± 0.29	17.06 ± 0.28
Tsagaan-Sol Moraine I	TGV-15-18 *	Be-10 (qtz)	**19.47 ± 0.37**	19.78 ± 0.37	19.32 ± 0.36	19.02 ± 0.36	18.83 ± 0.35	18.13 ± 0.34
Tsagaan-Sol Moraine I	TGV-15-19	Be-10 (qtz)	**17.49 ± 0.33**	17.85 ± 0.34	17.46 ± 0.33	17.09 ± 0.32	16.99 ± 0.32	16.38 ± 0.31
Tsagaan-Sol Moraine I	TGV-15-20 *	Be-10 (qtz)	**32.41 ± 0.71**	32.40 ± 0.71	31.50 ± 0.69	31.67 ± 0.70	30.75 ± 0.68	29.48 ± 0.65
Tsagaan-Sol Moraine I	TGV-15-21 *	Be-10 (qtz)	**14.44 ± 0.33**	14.87 ± 0.34	14.57 ± 0.33	14.11 ± 0.32	14.15 ± 0.32	13.69 ± 0.31
Tsagaan-Sol Moraine I	TGV-15-22 *	Be-10 (qtz)	**27.82 ± 0.48**	27.87 ± 0.48	27.14 ± 0.47	27.18 ± 0.47	26.50 ± 0.46	25.44 ± 0.44
Tsagaan-Sol Moraine I	TGV-15-23	Be-10 (qtz)	**17.87 ± 0.38**	18.23 ± 0.38	17.83 ± 0.37	17.46 ± 0.37	17.35 ± 0.36	16.73 ± 0.35
Tsagaan-Sol Moraine I	TGV-15-24 *	Be-10 (qtz)	**43.72 ± 0.66**	43.40 ± 0.65	42.15 ± 0.63	42.71 ± 0.64	41.26 ± 0.62	39.57 ± 0.59
Tsagaan-Sol Erratics	TGV-15-08	Be-10 (qtz)	**16.31 ± 0.35**	16.70 ± 0.36	16.36 ± 0.36	15.94 ± 0.35	15.89 ± 0.35	15.35 ± 0.33
Tsagaan-Sol Erratics	TGV-15-09	Be-10 (qtz)	**16.51 ± 0.31**	16.89 ± 0.32	16.54 ± 0.31	16.13 ± 0.30	16.08 ± 0.30	15.52 ± 0.29
Tsagaan-Sol Erratics	TGV-15-10	Be-10 (qtz)	**17.22 ± 0.32**	17.59 ± 0.33	17.22 ± 0.32	16.82 ± 0.32	16.74 ± 0.31	16.17 ± 0.30
Tsagaan-Sol Erratics	TGV-15-14	Be-10 (qtz)	**16.67 ± 0.27**	17.05 ± 0.28	16.69 ± 0.27	16.29 ± 0.27	16.23 ± 0.26	15.66 ± 0.26
Tsagaan-Sol Erratics	TGV-15-17	Be-10 (qtz)	**16.63 ± 0.27**	17.02 ± 0.28	16.65 ± 0.27	16.25 ± 0.26	16.20 ± 0.26	15.63 ± 0.25
Tsagaan-Sol Erratics	TGV-15-26	Be-10 (qtz)	**18.19 ± 0.34**	18.53 ± 0.35	18.12 ± 0.34	17.77 ± 0.33	17.64 ± 0.33	17.01 ± 0.32
Takhilt Valley Moraine I	TKLT-16-02	Be-10 (qtz)	**16.28 ± 0.32**	16.71 ± 0.32	15.90 ± 0.31	15.91 ± 0.31	15.90 ± 0.31	14.93 ± 0.29
Takhilt Valley Moraine I	TKLT-16-05	Be-10 (qtz)	**15.57 ± 0.32**	16.02 ± 0.33	15.21 ± 0.32	15.22 ± 0.32	15.25 ± 0.32	14.29 ± 0.30
Takhilt Valley Moraine I	TKLT-16-07	Be-10 (qtz)	**16.27 ± 0.31**	16.70 ± 0.31	15.82 ± 0.30	15.90 ± 0.30	15.90 ± 0.30	14.86 ± 0.28

Note. Samples marked by a single asterisk (*) next to the sample ID are considered outliers and are not included in statistical analyses. Bold ages are those discussed in the text.

Figure 9). A cluster of erratic boulders on thin drift near the eastern base of Biluut 1 afford an average age of 18,810 ± 80 (510) years (n = 3), whereas a cluster of erratic boulders located ~15 km up the valley from the Khoton Biluuts afford a mean age of 18,060 ± 210 (530) years (n = 5). Dates from a 4-km-long train of erratic boulders resting on the ice-molded bedrock ~5–10 km farther up valley in the Tsagaan-Sol Valley range from 18,190 ± 340 years to 16,310 ± 350 years. The outermost age of this boulder train is 18,190 ± 340 years, and it lies outboard of a moraine ridge containing a cluster of angular boulders (Figure 7). Ages from this moraine ridge yield a wide age range likely due to inherited inventories of ^{10}Be that were not effectively removed during glacial transport. Two morphostratigraphically consistent ages from this morainal boulder cluster yield an average age of 17,680 ± 190 (510) years (Tsagaan-Sol I; n = 7, −5 outliers). Erratic boulders associated with the 4-km boulder train located inboard of the moraine ridge range between 16,200 ± 400 and 17,200 ± 300 years old (Figure 7) and form an approximately normal distribution (Figure 8), indicating that the ages are statistically indistinguishable from each other. Finally, the innermost landform of the sequence, located ~5 km outboard of the late Holocene moraines of Takhilt Pass, affords a mean age of 16,040 ± 230 (490) years (Takhilt I; n = 3).

8. Discussion

Our glacial-geomorphic mapping and ^{10}Be surface-exposure dating show that the Khoton glacier achieved maximal phases at 35,440 ± 210 (980) years ago, 23,430 ± 570 (850) years ago, 20,780 ± 230 (610) years ago, and 19,520 ± 160 (550) years ago. Ages on erratic boulders indicate that glacier recession from Khoton Nuur was underway shortly after 18,810 ± 80 (510) years ago. By 17,680 ± 190 (510) years ago, the margin of the Khoton glacier had retreated to 50% of its maximal extent (Figure 10). Retreat to within 5 km of the pre-industrial ice

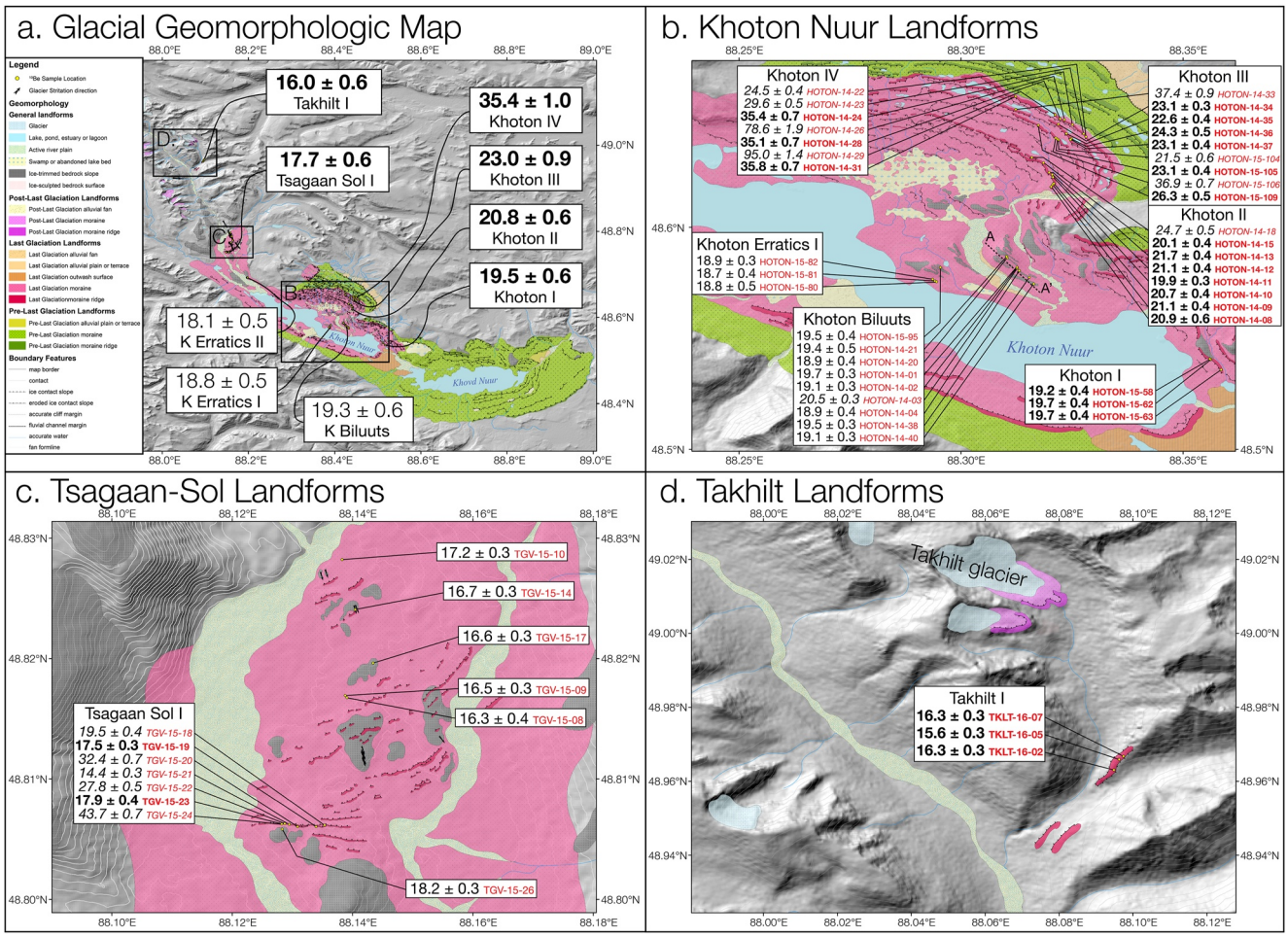

Figure 7. Glacial geomorphic maps of dated landforms with exposure ages (ages are in kyrs) and sample locations plotted. Bold-type exposure ages are from moraines, regular-type exposure ages are from glacial erratics, whereas italic-type exposure ages are those identified as outliers. Geomorphological symbols and map panel boundaries are equivalent to Figures 2 and 3.

margin was completed by 16,040 ± 230 (490) years ago, corresponding to an overall length reduction of 90% by this time (Figure 11).

We interpret length changes of the former Khoton glacier as reflecting glacier response to the past climate change. Although in some circumstances glacier length changes can exhibit a complex (i.e., nonlinear) relationship to corresponding ELA changes, glaciers with gently sloping, constant bed profiles (Figure 10) tend to exhibit a linear relationship between length and ELA (Doughty et al., 2017; Klok & Oerlemans, 2003, 2004; Mackintosh et al., 2017; Oerlemans, 2001, 2012; Putnam et al., 2012; Roe et al., 2017). Our chronology for the Khoton glacier indicates that the climate of western Mongolia had achieved maximal cooling and ELA lowering as early as ~35,000 years ago and again during subsequent glacier advances that culminated at ~23,000 years ago, ~20,800 years ago, and at ~19,500 years ago. Deglaciation then began shortly after ~18,800 years ago, heralding the termination of ice-age conditions in this part of Central Asia. Glacier withdrawal to near-present-day lengths by ~16,000 years ago indicates that the climate had warmed to near-interglacial temperatures by that time, signaling the onset of a near-interglacial climate mode within three millennia after the start of the local last glacial termination.

The younger three Khoton glacier maxima, 23,430 ± 570 (850) years ago, 20,780 ± 230 (610) years ago, and 19,520 ± 160 (550) years ago, coincided with low local summertime insolation intensities and atmospheric CO_2 concentrations (Figure 12). Coeval timing of maximal glacier extents, low summer insolation intensity, and low

Table 4
Summary Statistics for ^{10}Be Landform Ages

Data set	*n*	*n* out	Mean age (yrs)	±SEM uncertainty (yrs)	±"External" uncertainty (yrs)	±1σ (standard deviation) (yrs)	Peak age (yrs)	Median age (yrs)	χ^2	Reduced χ^2
Khoton Moraine IV (all)	7	-	47,700	10,360	10,400	27,400	35,400	35,400	6417.08	1069.51
Khoton Moraine IV (outliers excluded)	3	4	**35,440**	**210**	**980**	370	35,410	35,380	0.56	0.28
Khoton Moraine III (all)	9	-	26,500	2100	2200	6,200	23,100	23,100	790.35	98.79
Khoton Moraine III (outliers excluded)	7	2	**23,430**	**570**	**850**	1,520	23,060	23,110	53.02	8.84
Khoton Moraine II (all)	8	-	21,270	530	780	1,450	21,000	20,970	74.42	10.63
Khoton Moraine II (outlier excluded)	7	1	**20,780**	**230**	**610**	610	21,000	20,870	15.50	2.58
Khoton Moraine I	3	-	**19,520**	**160**	**550**	280	19,580	19,650	0.98	0.49
Khoton Biluuts (all)	9	-	19,390	170	550	520	19,170	19,430	18.36	2.29
Khoton Biluuts (outlier excluded)	8	1	**19,250**	**110**	**530**	310	19,170	19,250	5.55	0.79
Khoton Erratics I	3	-	**18,810**	**80**	**510**	140	18,830	18,810	0.36	0.18
Khoton Erratics II	5	-	**18,060**	**210**	**530**	470	18,220	18,200	7.57	1.89
Tsagaan-Sol Moraine I (all)	7	-	24,700	3,970	4,030	10,500	17,600	19,500	3,015.47	502.58
Tsagaan-Sol Moraine I (outliers excluded)	2	5	**17,680**	**190**	**510**	270	17,630	17,680	0.60	0.60
Takhilt Valley Moraine I	3	-	**16,040**	**230**	**490**	410	16,240	16,270	3.23	1.62

atmospheric CO_2 also corresponds with the lowest value of global sea level, which reflects when the Northern Hemisphere ice sheets maintained their maximum volumes and areal extents of the LGM (Figure 12). Taken in isolation, these particular moraine belts of the Khoton sequence were constructed coevally with decreased radiative forcing during the LGM (e.g., Marcott et al., 2019; Osman et al., 2021; Shakun et al., 2015; Tierney et al., 2020). This finding is in broad agreement with previous studies from Central Asia, demonstrating expansive mountain glaciers during the global LGM (Lehmkuhl et al., 2004, 2007, 2011, 2016; Batbaatar et al., 2018; Blomdin et al., 2016; Dong et al., 2020; Gribenski et al., 2016, 2018; Klinge et al., 2021; Yang et al., 2017). Additionally, deglaciation of the Khoton glacier after ~18,800 years ago was underway when radiative forcing at northern latitudes generally began to increase (Figure 12).

Although the timing of moraine construction in the Khoton Nuur valley is generally consistent with the hypothesis that radiative forcing was important for driving ice-age climate change, two problems arise when considering (a) the timing and rate of deglaciation of the Khoton glacier and (b) maximal ice extent during MIS 3. First, the Khoton Nuur chronology shows that the recession of the Khoton glacier, driven by summer melt, outpaced the rise of atmospheric CO_2 as well as any significant demise of the large northern sheets (as recorded by the rise of global sea level) by several thousand years (Figure 12). By 16,040 ± 230 (490) years ago when the Khoton glacier had retreated 90% of its full-glacial length to within 5 km of its pre-industrial margin at Takhilt Pass, global sea level (here taken as a proxy for the volume of Northern Hemisphere ice sheets) and atmospheric CO_2 concentrations had risen only slightly above their respective LGM minimum values (Figure 12). Likewise, the Khoton Nuur glacier system had receded to an interglacial position several millennia before the combined radiative effects of atmospheric CO_2 and ice-sheet albedo had achieved interglacial levels (Figure 13).

This signature for the termination is not isolated to western Mongolia. In the Kyrgyz Tian Shan, ~1,000 km to the southwest of Khoton Nuur, the Inylchek Glacier had receded to near its pre-industrial Late-Holocene position by 16,170 ± 470 years ago (n = 4, −2 outliers) as well (Lifton, Beel, et al., 2014). Farther afield in the European Alps, major ice-surface lowering was underway by no later than 17,700 ± 600 years ago (Wirsig, Zasadni, Christl, et al., 2016; Wirsig, Zasadni, Ivy-Ochs, et al., 2016) and retreat well into the mountain valleys had occurred by ~16,000–17,000 years ago (Amman & Lotter, 1989; Ivy-Ochs, 2015). Extensive alpine ice recession corresponded with enhanced meltwater delivery into the Danube River between 18,000 and 16,000 years ago

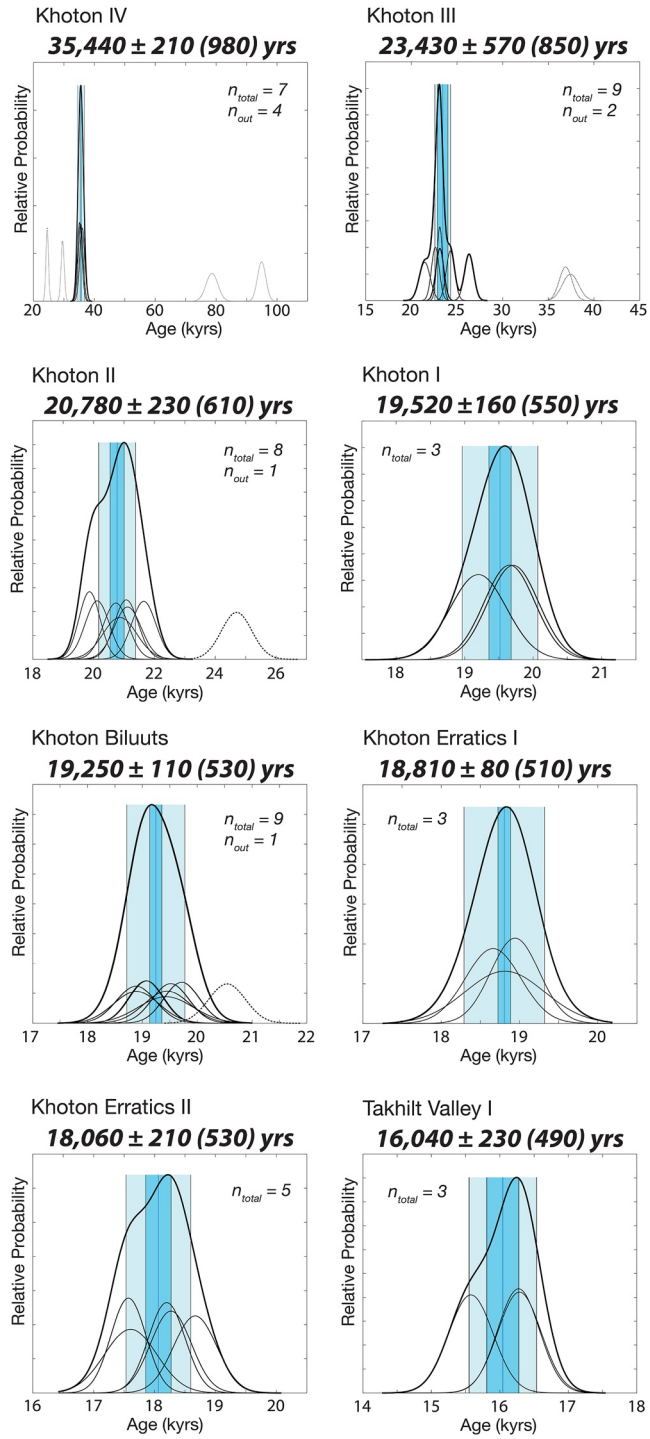

Figure 8. Normal kernel density functions (i.e., "camelplots") for landforms in the field area. Center blue line is arithmetic mean. Dark blue-shaded area represents the standard error of the mean (SEM) and the light blue-shaded area represents the "external uncertainty." The thin black curves are the Gaussian representation of each sample. Dotted black lines represent outliers. The thick black curve is the total probability distribution of all plotted samples, excluding outliers. Associated statistics for each population are presented in Table 4.

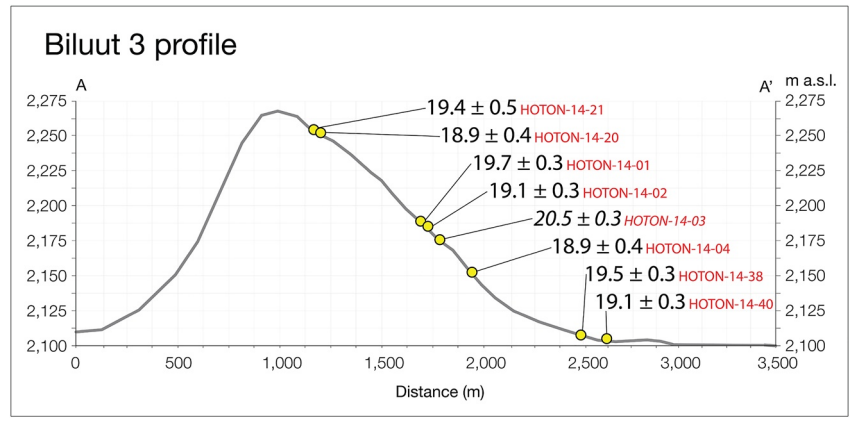

Figure 9. Profile showing the form of Biluut 3 with exposure ages plotted (ages are in kyrs). Location of profile transect is plotted (A to A') on map in Figures 3 and 7.

(Martinez-Lamas et al., 2020). Therefore, the chronology of ice recession documented at Khoton Nuur was a characteristic of a widespread signal registered among temperature-sensitive mountain-glacier systems elsewhere in Central Asia and in Europe. The observation that mountain glaciers in these regions receded to interglacial volumes several millennia before the disappearance of the Laurentide Ice Sheet, for example, indicates that summer warming in Eurasia overpowered any potential cooling that may have been afforded by albedo feedbacks imposed by the still-large Northern Hemisphere ice sheets between ~19,000 years ago and ~16,000 years ago (Figure 13).

Second, our chronology indicates that the Khoton Nuur glacier achieved a maximum extent at least as early as 35,000 years ago, nearly 10,000 years before the maximum in global ice volume, well before the lowest atmospheric CO_2 concentrations, and during a period of relatively high local summer insolation intensity (Figure 12). The Khoton Nuur chronology dovetails with other moraine chronologies that indicate extensive pre-LGM advances of Mongolian and Altai mountain glaciers (Blomdin et al., 2018; Dong et al., 2020; Gillespie et al., 2008; Gribenski et al., 2018; Klinge et al., 2021; Krivonogov et al., 2012; Lehmkuhl et al., 2011; Prokopenko et al., 2009; Rother et al., 2014). For example, a ^{10}Be chronology from the Otgon Tenger glacier cap in the Khangai Mountains of central Mongolia shows that moraine construction took place between and ~46,000 and 38,000 years ago (Rother et al., 2014), and a terminal moraine in the Bumbat Valley in the Hangai Ranges

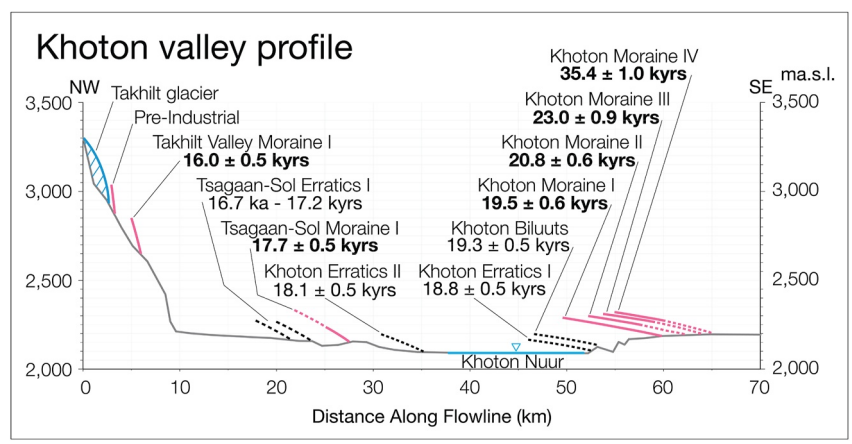

Figure 10. Khoton valley profile illustrating ice-surface profiles, with chronology (ages in kyrs), of the former Khoton glacier. Surface profiles are estimated based on lateral moraine profiles where available. Profiles based on lateral moraines are plotted in magenta, and profiles estimated for corresponding erratic boulders are plotted in black. A present-day glacier margin at the head of Takhilt Valley is illustrated in blue. Extrapolated profiles are shown as dotted lines. Vertical scale is exaggerated 50×.

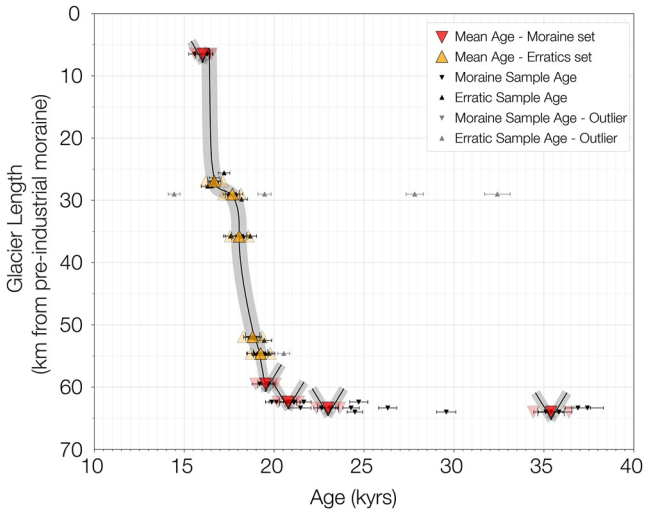

Figure 11. Time-distance diagram showing the retreat history of the former Khoton glacier. Exposure ages and uncertainties are plotted as triangles and horizontal bars, respectively. Symbols are described in legend, inset. Exposure ages marked as outliers are shown in gray coloring. Faded symbols represent moraine ages adjusted to the limits of uncertainty bounds attending the production-rate calibration data set. Gray line indicates a likely retreat history as constrained by exposure ages.

of central Mongolia was constructed between ~41,000 and 33,000 years ago (Batbaatar et al., 2018). Likewise, moraines were constructed between ~32,000 and 29,000 years ago in the Darhad Basin of northern Mongolia (Gillespie et al., 2008). Evidence for extensive glaciation during MIS 3 has also been demonstrated in the greater Altai region. For example, glaciers of the Ikh Turgen Mountains in the northern Altai sector deposited moraines between ~52,000 and 33,000 years ago (Blomdin et al., 2018), and a moraine was constructed at ~38,000 ± 2,200 years ago (n = 9) in the Xiaokelanhe River basin in the Chinese Altai (Dong et al., 2020). We note that these previously published ^{10}Be exposure-age data sets have been recalculated in a manner consistent with the ^{10}Be ages presented here for Khoton Nuur.

Next, we examine whether Mercer's Paradox applies to the Asian/Australasian sector of the planet as it did in the Americas (Mercer, 1984). Murphy (1869) and Milankovitch (1941) identified summer cooling caused by orbitally induced changes in summer insolation as the key driver of glaciation. If true however, then glacier fluctuations should have been out of phase between midlatitudes of the two polar hemispheres. Our chronology shows that the Khoton glacier, located near the center of the large Asian continent, achieved maximal extents coevally with mountain glaciers in the Southern Alps of New Zealand (~43°–44°S), situated within the southwest Pacific Ocean (Doughty et al., 2015; Kelley et al., 2014; Putnam, Schaefer, Denton, Barrell, Birkel, et al., 2013; Rother et al., 2015; Schaefer et al., 2015; Strand et al., 2019; Figure 14). Likewise, extensive glacier recession took place nearly simultaneously between ~18,000 years ago and ~16,000 years ago in the Altai (this study) and in the Southern Alps (Putnam, Schaefer, Denton, Barrell, Andersen, et al., 2013) despite being in opposite hemispheres and situated in different climatic settings, further highlighting Mercer's Paradox.

The most rapid phase of deglaciation in each of these midlatitude sites occurred during the early millennia of Heinrich Stadial 1 (~17,800–14,700 years ago). During this time, enhanced meltwater and iceberg fluxes stratified the North Atlantic Ocean (Barker & Diz, 2014; Barker et al., 2009, 2015; Toucanne et al., 2015), leading to extensive winter sea-ice growth and depressed mean-annual temperatures registered in the circum-North Atlantic region (Bard et al., 2000; McManus et al., 1994; Rasmussen et al., 2016). On the other hand, observations of extensive melt and glacier recession in the European Alps and Mongolian Altai indicate intensified summertime warming during this time. Taken together, observations of cool, stratified surface-ocean conditions in the North Atlantic, cold mean-annual temperatures, and accelerated ice terrestrial mountain-glacier recession are most easily reconciled by the consideration that intense seasonality, with warm summers and hypercold winters, characterized the climate of the North Atlantic during Heinrich Stadial 1 (Denton et al., 2005, 2010, 2021).

In sum, the mountain glacier reconstruction from the Mongolian Altai presented here reveals the emergence of Mercer's Paradox in the Asian/Australasian sector of the planet, calling into question the simple application of northern-latitude summer orbital forcing as a driver of global ice-age climate (e.g., Milankovitch, 1941) as noted by Mercer (1984, 1976). These considerations suggest that a different linkage between orbital forcing and global ice-age climate change is required, one in which the resulting global climate drives glaciers simultaneously in both polar hemispheres. While various combinations of rising atmospheric CO_2 and insolation-driven ice-sheet feedbacks have been invoked to explain global warming and near-global glacier recession during the last glacial termination (Broecker, 2014; Osman et al., 2021; Shakun et al., 2012, 2015; Tierney et al., 2020), these radiative forcing factors fail to explain the rapid, nonlinear recession of midlatitude mountain glacier systems in Central Asia and the Southern Alps from glacial to interglacial modes that took place during Heinrich Stadial 1. We suggest that an additional heating agent is required to explain how ice loss outpaced typical radiative forcing agents at least in the midlatitude locations considered here. In other words, any solution to the ice-age puzzle will

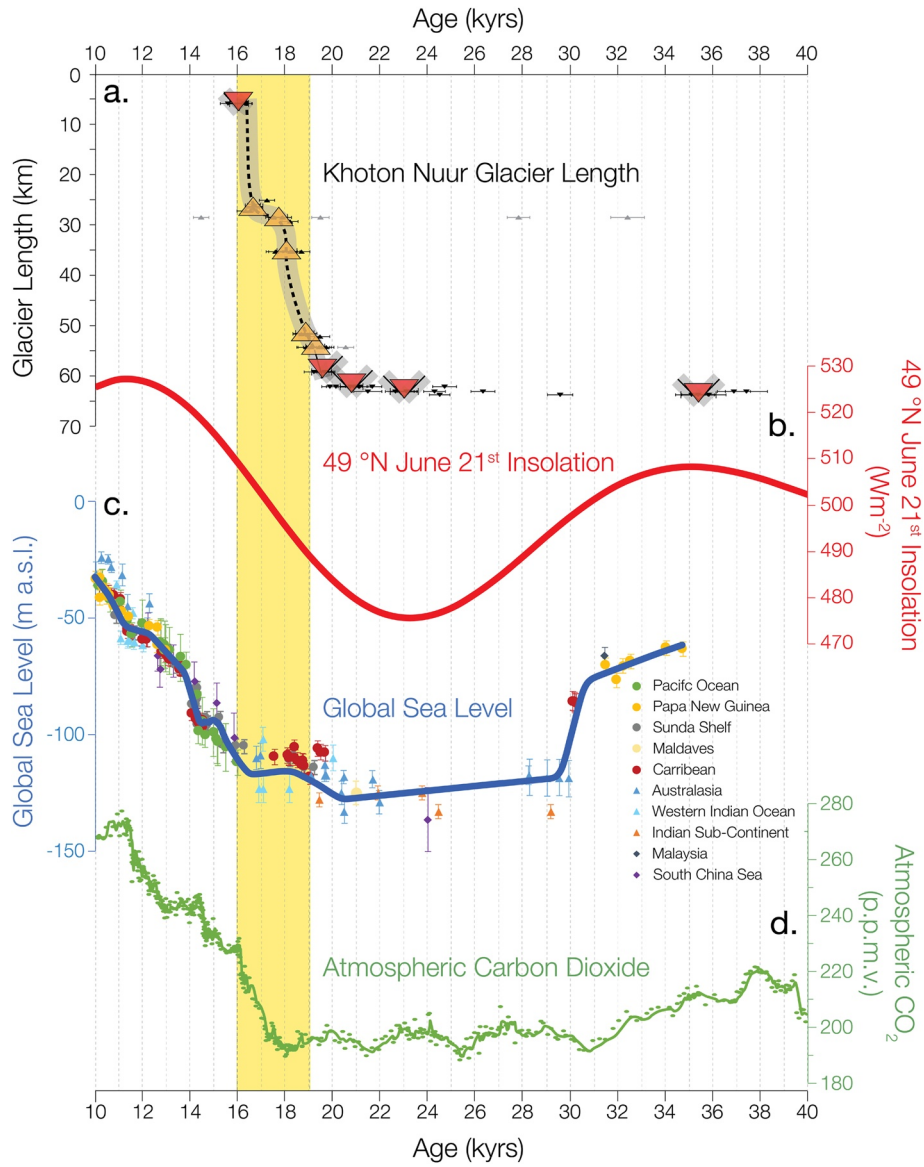

Figure 12. Time-distance diagram showing the retreat history of the former Khoton glacier plotted against global climate drivers discussed in the text. (a) Khoton glacier time-distance diagram from Figure 11. (b) Local summertime insolation intensity calculated for June 21st at 49°N. (c) Global sea level, an analog for global ice volume (data compiled in Lambeck et al., 2014). (d) Atmospheric CO_2 concentration as measured in Antarctic ice cores (Bauska et al., 2021; Buizert et al., 2015; Marcott et al., 2014).

need to account for coeval glacial maxima, and rapid, simultaneous deglaciation in interior Asia and the middle latitudes of the Southern Hemisphere. Further development of detailed glacier chronologies documenting the Last Glaciation and last glacial termination in both polar hemispheres, in continental and oceanic climate settings, will help to elucidate a solution to the global ice-age problem.

9. Conclusions

Our ^{10}Be surface-exposure ages from glacial landforms in the Mongolian Altai demonstrate that Mercer's Paradox applies to the Asian/Australasian sector of the globe in the same fashion as Mercer (1984) established for North and South America. Although Khoton glacier maxima coincided with the global LGM

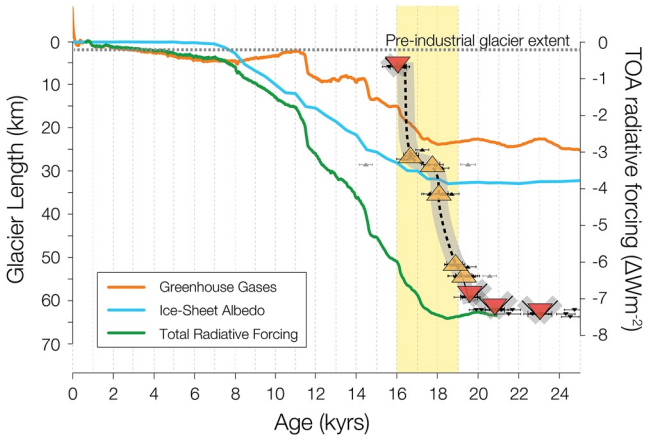

Figure 13. Time-distance diagram showing the retreat history of the former Khoton glacier plotted against top of atmosphere radiative forcing (data compiled by Baggenstos et al., 2019). Vertical yellow band represents the duration of deglaciation of Khoton Nuur. This comparison shows that the Khoton Nuur glacier had receded to a near-interglacial position well before these common radiative forcing agents had achieved interglacial values.

(~26.5–19.0 ka), a direct correlation with proposed global climate drivers, such as summer insolation intensity at northern latitudes, does not adequately account for the full glacier chronology presented here. Furthermore, the record of Khoton glacier retreat shows that the rise of summer temperatures in the Mongolian Altai to interglacial values led to the demise of the large northern sheets as well as the rise of atmospheric CO_2 by several thousand years. This leads us to ask: If full-glacial climate in Mongolia reverted to a near-interglacial climate condition with relatively small contributions from rising atmospheric CO_2 and a slight reduction in Northern Hemisphere ice-sheet size, was any combination of insolation intensity, ice sheet size, and low atmospheric CO_2 sufficient to drive Northern Hemisphere glaciation in the first place? Could another factor, one sufficiently strong to overpower the more gradual effects of these forcing factors, be necessary for explaining the nonlinear pace of mountain-glacier recession during the termination? Further development of precise mountain glacier records from auxiliary locations around the globe will help to fully resolve these questions.

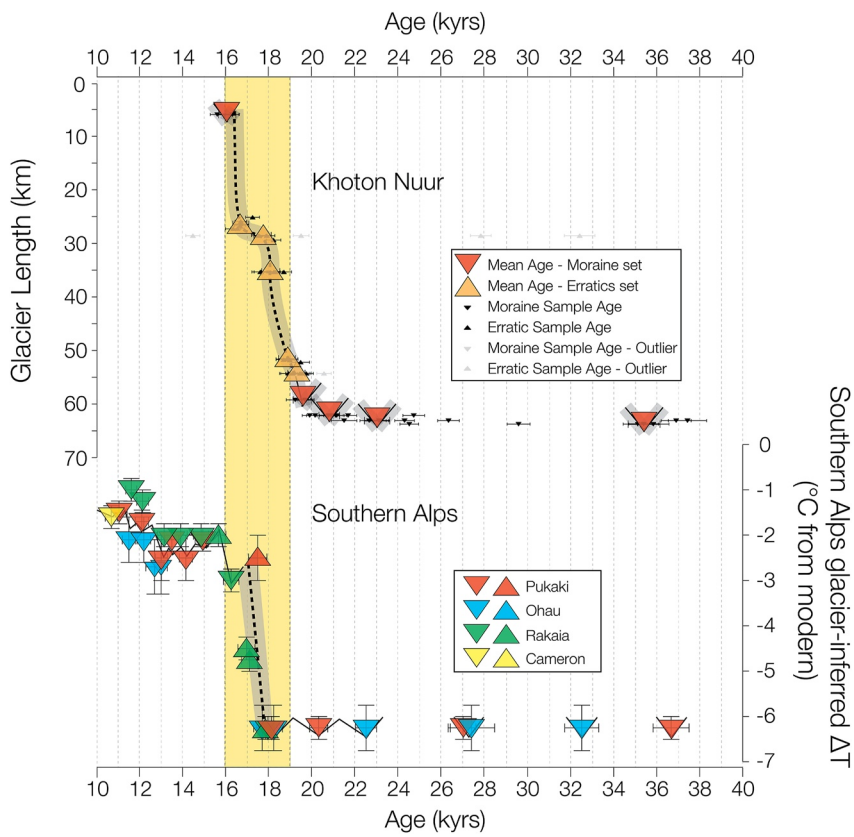

Figure 14. Khoton Nuur glacier length (49°N) compared with glacier-inferred temperatures developed from Southern Alps glacier chronologies (Denton et al., 2021; Doughty et al., 2015; Kelley et al., 2014; Putnam, Schaefer, Denton, Barrell, Andersen, et al., 2013; Putnam, Schaefer, Denton, Barrell, Birkel, et al., 2013; Schaefer et al., 2015; Strand et al., 2019).

Data Availability Statement

^{10}Be sample details, analytical data, and exposure ages from this study are available at the NOAA NCEI Paleoclimatology repository via Strand et al. (2022).

Acknowledgments
This research was supported by a National Science Foundation CAREER award to Aaron Putnam (EAR-1594990), as well as funding from the Quesada Family Fund and the Comer Science and Education Foundation. We thank Altai Tavn Bogd National Park for granting us permission to carry out fieldwork in the Khoton Nuur region. We thank Olaf Jensen, Peter Quesada, Henry Quesada, Scott Travis, Destiny Washington, Patricia Joyner, Caleb Ward, Nate Norris, Tumur Batbold, Oroza Seribol, Tsetsee Bavuu, Ninjin Tsolmon, Oochko Purevdorj, Richard Kortum, and Tanzhuo Liu for their help in the field, and Roseanne Schwartz, Jeremy Frisch, and Jean Hanley for assistance with laboratory work at Lamont. We are extremely grateful to Uyanga Bold, Jagaa, Gantuaga, Boldoo Baatar, Bagi Gurkhlaajar, and the entire team at Hovsgol Travel for making our Mongolia expeditions possible. This is LDEO contribution #XXXX.

References

Ageta, Y., & Higuchi, K. (1984). Estimation of mass balance components of a summer-accumulation type glacier in the Nepal Himalaya. *Geografiska Annaler - Series A: Physical Geography*, *66*(3), 249–255. https://doi.org/10.2307/520698

Amman, B., & Lotter, A. F. (1989). Late-glacial radiocarbon and palynostratigraphy on the Swiss Plateau. *Boreas*, 109–126.

Andersen, B. G., Denton, G. H., & Lowell, T. V. (1999). Glacial geomorphologic maps of Llanquihue drift in the area of the Southern Lake District, Chile. *Geografiska Annaler Series A Physical Geography*, *81*(2), 155–166. https://doi.org/10.1111/j.0435-3676.1999.00056.x

Anderson, B. M., & Mackintosh, A. N. (2006). Temperature change is the major driver of late-glacial and Holocene glacier fluctuations in New Zealand. *Geology*, *34*(2), 121. https://doi.org/10.1130/g22151.1

Anderson, B. M., Mackintosh, A. N., Stumm, D., George, L., Kerr, T., Winter-Billington, A., & Fitzsimons, S. J. (2010). Climate sensitivity of a high-precipitation glacier in New Zealand. *Journal of Glaciology*, *56*(195), 114–128. https://doi.org/10.3189/002214310791190929

Baggenstos, D., Häberli, M., Schmitt, J., Shackleton, S. A., Birner, B., Severinghaus, J. P., et al. (2019). Earth's radiative imbalance from the Last Glacial Maximum to the present. *Proceedings of the National Academy of Sciences*, *116*(30), 14881–14886. https://doi.org/10.1073/pnas.1905447116

Balco, G. (2017). Production rate calculations for cosmic-ray-muon-produced 10Be and 26Al benchmarked against geological calibration data. *Quaternary Geochronology*, *39*, 150–173. https://doi.org/10.1016/j.quageo.2017.02.001

Balco, G., Briner, J. P., Finkel, R. C., Rayburn, J. A., Ridge, J. C., & Schaefer, J. M. (2009). Regional beryllium-10 production rate calibration for late-glacial northeastern North America. *Quaternary Geochronology*, *4*, 93–107.

Balco, G., Purvance, M. D., & Rood, D. H. (2011). Exposure dating of precariously balanced rocks. *Quaternary Geochronology*, *6*(3–4), 295–303. https://doi.org/10.1016/j.quageo.2011.03.007

Balco, G., Stone, J. O., Lifton, N. A., & Dunai, T. J. (2008). A complete and easily accessible means of calculating surface exposure ages or erosion rates from 10Be and 26Al measurements. *Quaternary Geochronology*, *3*, 174–195. https://doi.org/10.1016/j.quageo.2007.12.001

Bard, E., Rostek, F., Turon, J.-L., & Gendreau, S. (2000). Hydrological impact of Heinrich events in the subtropical northeast Atlantic. *Science 84*, *289*(5483), 1321–1324. https://doi.org/10.1126/science.289.5483.1321

Barker, S., Chen, J., Gong, X., Jonkers, L., Knorr, G., & Thornalley, D. (2015). Icebergs not the trigger for North Atlantic cold events. *Nature*, *520*(7547), 333–336. https://doi.org/10.1038/nature14330

Barker, S., & Diz, P. (2014). Timing of the descent into the last Ice Age determined by the bipolar seesaw. *Paleoceanography*, *29*(6), 489–507. https://doi.org/10.1002/2014PA002623

Barker, S., Diz, P., Vautravers, M. J., Pike, J., Knorr, G., Hall, I. R., & Broecker, W. S. (2009). Interhemispheric Atlantic seesaw response during the last deglaciation. *Nature*, *457*(7233), 1097–1102. https://doi.org/10.1038/nature07770

Batbaatar, J., Gillespie, A. R., Fink, D., Matmon, A., & Fujioka, T. (2018). Asynchronous glaciations in arid continental climate. *Quaternary Science Reviews*, *182*, 1–19. https://doi.org/10.1016/j.quascirev.2017.12.001

Bauska, T. K., Marcott, S. A., & Brook, E. J. (2021). Abrupt changes in the global carbon cycle during the last glacial period. *Nature Geoscience*, *14*(2), 91–96. https://doi.org/10.1038/s41561-020-00680-2

Blomdin, R., Heyman, J., Stroeven, A. P., Hättestrand, C., Harbor, J. M., Gribenski, N., et al. (2016). Glacial geomorphology of the Altai and Western Sayan Mountains, Central Asia. *Journal of Maps*, *12*(1), 123–136. https://doi.org/10.1080/17445647.2014.992177

Blomdin, R., Stroeven, A. P., Harbor, J. M., Gribenski, N., Caffee, M. W., Heyman, J., et al. (2018). Timing and dynamics of glaciation in the Ikh Turgen mountains, Altai region, high Asia. *Quaternary Geochronology*, *47*, 54–71. https://doi.org/10.1016/j.quageo.2018.05.008

Borchers, B., Marrero, S., Balco, G., Caffee, M., Goehring, B., Lifton, N., et al. (2016). Geological calibration of spallation production rates in the CRONUS-Earth project. *Quaternary Geochronology*, *31*, 188–198. https://doi.org/10.1016/j.quageo.2015.01.009

Broecker, W. (1978). The cause of glacial to interglacial climatic change. In *Evolution of planetary atmospheres and climatology of the Earth*.

Broecker, W. (2014). *Wally's carbon world*.

Broecker, W. S. (1966). Absolute dating and the astronomical theory of glaciation. *Science*, *151*(3708), 299–304. https://doi.org/10.1126/science.151.3708.299

Broecker, W. S., & van Donk, J. (1970). Insolation changes, ice volumes, and the O18 record in deep-sea cores. *Review of Geophysics*, *8*(1), 169–198. https://doi.org/10.1029/rg008i001p00169

Buizert, C., Cuffey, K. M., Severinghaus, J. P., Baggenstos, D., Fudge, T. J., Steig, E. J., et al. (2015). The WAIS Divide deep ice core WD2014 chronology—Part 1: Methane synchronization (68–31 ka BP) and the gas age-ice age difference. *Climate of the Past*, *11*(2), 153–173. https://doi.org/10.5194/cp-11-153-2015

Clark, P. U., Dyke, A. S., Shakun, J. D., Carlson, A. E., Clark, J., Wohlfarth, B., et al. (2009). The last glacial maximum. *Science*, *325*(5941), 710–714. https://doi.org/10.1126/science.1172873

Clark, P. U., & Mix, A. C. (2002). Ice sheets and sea level of the Last Glacial Maximum. *Quaternary Science Reviews*, *21*(1–3), 1–7. https://doi.org/10.1016/s0277-3791(01)00118-4

Denton, G. H., Alley, R. B., Comer, G. C., & Broecker, W. S. (2005). The role of seasonality in abrupt climate change. *Quaternary Science Reviews*, *24*(10–11), 1159–1182. https://doi.org/10.1016/j.quascirev.2004.12.002

Denton, G. H., Anderson, R. F., Toggweiler, J. R., Edwards, R. L., Schaefer, J. M., & Putnam, A. E. (2010). The last glacial termination. *Science 84*, *328*(5986), 1652–1656. https://doi.org/10.1126/science.1184119

Denton, G. H., Putnam, A. E., Russell, J. L., Barrell, D. J. A., Schaefer, J. M., Kaplan, M. R., & Strand, P. D. (2021). The Zealandia switch: Ice Age climate shifts viewed from Southern Hemisphere moraines. *Quaternary Science Reviews*, *257*, 106771. https://doi.org/10.1016/j.quascirev.2020.106771

Dong, G., Zhou, W., Fu, Y., Zhang, L., Zhao, G., & Li, M. (2020). The last glaciation in the headwater area of the Xiaokelanhe River, Chinese Altai: Evidence from 10Be exposure-ages. *Quaternary Geochronology*, *56*, 101054. https://doi.org/10.1016/j.quageo.2020.101054

Doughty, A. M., Mackintosh, A. N., Anderson, B. M., Dadic, R., Putnam, A. E., Barrell, D. J. A., et al. (2017). An exercise in glacier length modeling: Interannual climatic variability alone cannot explain Holocene glacier fluctuations in New Zealand. *Earth and Planetary Science Letters*, *470*, 48–53. https://doi.org/10.1016/j.epsl.2017.04.032

Doughty, A. M., Schaefer, J. M., Putnam, A. E., Denton, G. H., Kaplan, M. R., Barrell, D. J., et al. (2015). Mismatch of glacier extent and summer insolation in Southern Hemisphere mid-latitudes. *Geology*, *43*(5), 407–410. https://doi.org/10.1130/g36477.1

Fitzhugh, W. W. (2011). The Mongolian deer Stone-Khirigsuur complex: Dating and organization of a late Bronze age menagerie. *Current archaeological research in Mongolia: Papers from the first International conference on "Archaeological Research in Mongolia" held in Ulaanbaatar*. August 19th-23rd, 2007 183–199.

Ganiushkin, D., Chistyakov, K., & Kunaeva, E. (2015). Fluctuation of glaciers in the southeast Russian Altai and northwest Mongolia mountains since the Little Ice Age maximum. *Environmental Earth Sciences*, *74*(3), 1883–1904. https://doi.org/10.1007/s12665-015-4301-2

Ganyushkin, D. A., Chistyakov, K. V., Volkov, I. V., Bantcev, D. V., Kunaeva, E. P., Andreeva, T. A., et al. (2018). Present glaciers of Tavan Bogd massif in the Altai Mountains, central Asia, and their changes since the Little Ice Age. *Geosciences*. https://doi.org/10.3390/geosciences8110414

Gillespie, A. R., Burke, R. M., Komatsu, G., & Bayasgalan, A. (2008). Late Pleistocene glaciers in Darhad basin, northern Mongolia. *Quaternary Research*, *69*(2), 169–187. https://doi.org/10.1016/j.yqres.2008.01.001

Gribenski, N., Jansson, K. N., Lukas, S., Stroeven, A. P., Harbor, J. M., Blomdin, R., et al. (2016). Complex patterns of glacier advances during the late glacial in the Chagan Uzun Valley, Russian Altai. *Quaternary Science Reviews*, *149*, 288–305. https://doi.org/10.1016/j.quascirev.2016.07.032

Gribenski, N., Jansson, K. N., Preusser, F., Harbor, J. M., Stroeven, A. P., Trauerstein, M., et al. (2018). Re-evaluation of MIS 3 glaciation using cosmogenic radionuclide and single grain luminescence ages, Kanas Valley, Chinese Altai. *Journal of Quaternary Science*, *33*(1), 55–67. https://doi.org/10.1002/jqs.2998

Hays, J. D., Imbrie, J., & Shackleton, N. J. (1976). Variations in the Earth's orbit: Pacemaker of the IceAges. *Science*, *194*(4270), 1121–1132. https://doi.org/10.1126/science.194.4270.1121

Hock, R., Bliss, A., Marzeion, B. E. N., Giesen, R. H., Hirabayashi, Y., Huss, M., et al. (2019). GlacierMIP—A model intercomparison of global-scale glacier mass-balance models and projections. *Journal of Glaciology*, *65*(251), 453–467. https://doi.org/10.1017/jog.2019.22

Hugonnet, R., McNabb, R., Berthier, E., Menounos, B., Nuth, C., Girod, L., et al. (2021). Accelerated global glacier mass loss in the early twenty-first century. *Nature*, *592*(7856), 726–731. https://doi.org/10.1038/s41586-021-03436-z

Imbrie, J., & Imbrie, J. Z. (1980). Modeling the climatic response to orbital variations. *Science*, *207*(4434), 943–953. https://doi.org/10.1126/science.207.4434.943

Ivy-Ochs, S. (2015). Variaciones glaciares en los Alphs europoes al final de la última glaciación. *Cuadernos de Investigacion Geografia*, *41*(2), 295–315. https://doi.org/10.18172/cig.2750

Jacobson-Tepfer, E. (2013). Late Pleistocene and early Holocene rock art from the Mongolian Altai: The material and its cultural implications. *Arts*, *2*(3), 151–181. https://doi.org/10.3390/arts2030151

Kamp, U., & Pan, C. G. (2015). Inventory of glaciers in Mongolia, derived from Landsat Imagery from 1989 to 2011. *Geografiska Annaler - Series A: Physical Geography*, *97*(4), 653–669. https://doi.org/10.1111/geoa.12105

Kawatra, S. K., & Eisele, T. C. (1992). 1 froth flotation—Fundamental principles. In *Recovery of pyrite in coal flotation: Entrainment or hydrophobicity?*

Kelley, S. E., Kaplan, M. R., Schaefer, J. M., Andersen, B. G., Barrell, D. J. A., Putnam, A. E., et al. (2014). High-precision 10Be chronology of moraines in the Southern Alps indicates synchronous cooling in Antarctica and New Zealand 42,000 years ago. *Earth and Planetary Science Letters*, *405*, 194–206. https://doi.org/10.1016/j.epsl.2014.07.031

Khalzan, P., Sakai, A., & Fujita, K. (2022). Mass balance of four Mongolian glaciers: In-situ measurements, long-term reconstruction and sensitivity analysis. *Frontiers of Earth Science*, *9*, 1–16. https://doi.org/10.3389/feart.2021.785306

Klinge, M., Schlutz, F., Zander, A., Hulle, D., Batkhishig, O., & Lehmkuhl, F. (2021). Late Pleistocene lake level, glaciation and climate change in the Mongolian Altai deduced from sedimentological and palynological archives. *Quaternary Research*, *99*, 168–189. https://doi.org/10.1017/qua.2020.67

Klok, E. J., & Oerlemans, J. (2003). Deriving historical equilibrium-line altitudes from a glacier length record by linear inverse modelling. *The Holocene*, *13*(3), 343–351. https://doi.org/10.1191/0959683603hl627rp

Klok, E. J., & Oerlemans, J. (2004). Climate reconstructions derived from global glacier length records. *Arctic Antarctic and Alpine Research*, *36*, 5752–6583. https://doi.org/10.1657/1523-0430(2004)036[0575:CRDFGG]2.0

Konya, K., Kadota, T., Davaa, G., Yabuki, H., & Ohata, T. (2010). Meteorological and ablation features of Potanin Glacier, Mongolian Altai. *Bulletin of Glaciological Research*, *28*, 7–16. https://doi.org/10.5331/bgr.28.7

Konya, K., Kadota, T., Nakazawa, F., Davaa, G., Purevdagva, K., Yabuki, H., & Ohata, T. (2013). Surface mass balance of the Potanin glacier in the Mongolian Altai Mountains and comparison with Russian Altai glaciers in 2005, 2008, and 2009. *Bulletin of Glaciological Research*, *31*(0), 9–18. https://doi.org/10.5331/bgr.31.9

Kortum, R. (2014). Sacred imagery and ritual landscape: New discoveries at the Biluut Petroglyph complex in the Mongolian Altai. *Time & Mind*, *7*(4), 329–384. https://doi.org/10.1080/1751696x.2014.969506

Krivonogov, S. K., Yi, S., Kashiwaya, K., Kim, J. C., Narantsetseg, T., Oyunchimeg, T., et al. (2012). Solved and unsolved problems of sedimentation, glaciation and paleolakes of the Darhad Basin, Northern Mongolia. *Quaternary Science Reviews*, *56*, 142–163. https://doi.org/10.1016/j.quascirev.2012.08.013

Lal, D. (1991). Cosmic ray labeling of erosion surfaces: In situ nuclide production rates and erosion models. *Earth and Planetary Science Letters*, *104*(2–4), 424–439. https://doi.org/10.1016/0012-821x(91)90220-c

Lambeck, K., Rouby, H., Purcell, A., Sun, Y., & Sambridge, M. (2014). Sea level and global ice volumes from the last glacial maximum to the Holocene. *Proceedings of the National Academy of Sciences*, *111*(43), 15296–15303. https://doi.org/10.1073/pnas.1411762111

Lehmkuhl, F., Klinge, M., Rother, H., & Hülle, D. (2016). Distribution and timing of Holocene and late Pleistocene glacier fluctuations in western Mongolia. *Annals of Glaciology*, *57*(71), 169–178. https://doi.org/10.3189/2016aog71a030

Lehmkuhl, F., Klinge, M., & Stauch, G. (2004). The extent of late Pleistocene glaciations in the Altai and Khangai mountains. *Developments in Quaternary Science*, 243–254. https://doi.org/10.1016/s1571-0866(04)80130-1

Lehmkuhl, F., Klinge, M., & Stauch, G. (2011). The extent and timing of late Pleistocene glaciations in the Altai and neighbouring mountain systems. *Developments in Quaternary Science*, *15*, 967–979. https://doi.org/10.1016/B978-0-444-53447-7.00069-6

Lehmkuhl, F., Zander, A., & Frechen, M. (2007). Luminescence chronology of fluvial and aeolian deposits in the Russian Altai (Southern Siberia). *Quaternary Geochronology*, *2*(1–4), 195–201. https://doi.org/10.1016/j.quageo.2006.04.005

Lifton, N., Beel, C., Hättestrand, C., Kassab, C., Rogozhina, I., Heermance, R., et al. (2014). Constraints on the late Quaternary glacial history of the Inylchek and Sary-Dzaz valleys from in situ cosmogenic ^{10}Be and ^{26}Al, eastern Kyrgyz Tian Shan. *Quaternary Science Reviews*, *101*, 77–90. https://doi.org/10.1016/j.quascirev.2014.06.032

Lifton, N., Sato, T., & Dunai, T. J. (2014). Scaling in situ cosmogenic nuclide production rates using analytical approximations to atmospheric cosmic-ray fluxes. *Earth and Planetary Science Letters*, *386*, 149–160. https://doi.org/10.1016/j.epsl.2013.10.052

Lifton, N. A., Phillips, F. M., & Cerling, T. E. (2016). Chapter 9—Using Lake Bonneville features to calibrate in situ cosmogenic nuclide production rates. In C. G. Oviatt, & J. F. B. T.-D. Shroder (Eds.), *Lake Bonneville* (pp. 165–183). Elsevier. https://doi.org/10.1016/B978-0-444-63590-7.00009-3

Lisiecki, L. E., & Raymo, M. E. (2005). A Pliocene-Pleistocene stack of 57 globally distributed benthic δ 18O records. *Paleoceanography*, *20*. https://doi.org/10.1029/2004pa001071

Litt, M., Shea, J., Wagnon, P., Steiner, J., Koch, I., Stigter, E., & Immerzeel, W. (2019). Glacier ablation and temperature indexed melt models in the Nepalese Himalaya. *Scientific Reports*, *9*, 1–13. https://doi.org/10.1038/s41598-019-41657-5

Mackintosh, A. N., Anderson, B. M., & Pierrehumbert, R. T. (2017). Reconstructing climate from glaciers. *Annual Review of Earth and Planetary Sciences*, *45*(1), 649–680. https://doi.org/10.1146/annurev-earth-063016-020643

Marcott, S. A., Bauska, T. K., Buizert, C., Steig, E. J., Rosen, J. L., Cuffey, K. M., et al. (2014). Centennial-scale changes in the global carbon cycle during the last deglaciation. *Nature*, *514*(7524), 616–619. https://doi.org/10.1038/nature13799

Marcott, S. A., Clark, P. U., Shakun, J. D., Brook, E. J., Davis, P. T., & Caffee, M. W. (2019). ^{10}Be age constraints on latest Pleistocene and Holocene cirque glaciation across the western United States. *Npj Climate and Atmospheric Science*, *2*(1), 5. https://doi.org/10.1038/s41612-019-0062-z

Martinez-Lamas, R., Toucanne, S., Debret, M., Riboulot, V., Deloffre, J., Boissier, A., et al. (2020). Linking Danube River activity to Alpine Ice-Sheet fluctuations during the last glacial (ca. 33–17 ka BP): Insights into the continental signature of Heinrich Stadials. *Quaternary Science Reviews*, *229*, 106136. https://doi.org/10.1016/j.quascirev.2019.106136

McKinnon, K. A., Stine, A. R., & Huybers, P. (2013). The spatial structure of the annual cycle in surface temperature: Amplitude, phase, and Lagrangian history. *Journal of Climate*, *26*(20), 7852–7862. https://doi.org/10.1175/jcli-d-13-00021.1

McManus, J. F., Bond, G. C., Broecker, W. S., Johnsen, S., Labeyrie, L., & Higgins, S. (1994). High-resolution climate records from the North-Atlantic during the last interglacial. *Nature*, *371*(6495), 326–329. https://doi.org/10.1038/371326a0

Mercer, J. H. (1976). Glacial history of southernmost South America. *Quaternary Research*, *6*(2), 125–166. https://doi.org/10.1016/0033-5894(76)90047-8

Mercer, J. H. (1984). Simultaneous climatic change in both hemispheres and similar bipolar interglacial warming: Evidence and implications. *Climate Processes and Climate Sensitivity*, *29*, 307–313. https://doi.org/10.1029/gm029p0307

Milankovitch, M. (1941). *Kanon der Erdbestrahlung und seine Anwendung auf das Eiszeitenproblem, Königliche Serbische Akademie*. Royal Serbian Academy.

Mix, A. C., Bard, E., & Schneider, R. (2001). Environmental processes of the ice age: Land, oceans, glaciers (EPILOG). *Quaternary Science Reviews*, *20*(4), 627–657. https://doi.org/10.1016/s0277-3791(00)00145-1

Murphy, J. J. (1869). On the nature and cause of the glacial climate. *Quarterly Journal of the Geological Society of London*, *25*(1–2), 350–356. https://doi.org/10.1144/GSL.JGS.1869.025.01-02.63

Nakazawa, F., Konya, K., Kadota, T., & Ohata, T. (2012). Reconstruction of the depositional environment upstream of Potanin Glacier, Mongolian Altai, from pollen analysis. *Environmental Research Letters*, *7*(3), 035402. https://doi.org/10.1088/1748-9326/7/3/035402

Nakazawa, F., Konya, K., Kadota, T., & Ohata, T. (2015). Depositional and summer snow melting features in 2007–2011 on the upstream side of Potanin Glacier, Mongolian Altai, reconstructed by pollen and oxygen isotope analysis. *Environmental Earth Sciences*, *74*(3), 1851–1859. https://doi.org/10.1007/s12665-015-4436-1

Nishiizumi, K., Imamura, M., Caffee, M. W., Southon, J. R., Finkel, R. C., & McAninch, J. (2007). Absolute calibration of 10Be AMS standards. *Nuclear Instruments and Methods in Physics Research Section B: Beam Interactions with Materials and Atoms*, *258*(2), 403–413. https://doi.org/10.1016/j.nimb.2007.01.297

Oerlemans, J. (1994). Quantifying global warming from the retreat of glaciers. *Science*, *264*(5156), 243–245. https://doi.org/10.1126/science.264.5156.243

Oerlemans, J. (2001). *Glaciers and climate change*. CRC Press.

Oerlemans, J. (2005). Extracting a climate signal from 169 glacier records. *Science*, *80*(5722), 675–677. https://doi.org/10.1126/science.1107046

Oerlemans, J. (2012). Linear modelling of glacier length fluctuations. *Geografiska Annaler Series A Physical Geography*, *94*(2), 183–194. https://doi.org/10.1111/j.1468-0459.2012.00469.x

Osman, M. B., Tierney, J. E., Zhu, J., Tardif, R., Hakim, G. J., King, J., & Poulsen, C. J. (2021). Globally resolved surface temperatures since the Last Glacial Maximum. *Nature*, *599*(7884), 2–53. https://doi.org/10.1038/s41586-021-03984-4

Peltier, W. R., & Fairbanks, R. G. (2006). Global glacial ice volume and Last Glacial Maximum duration from an extended Barbados sea level record. *Quaternary Science Reviews*, *25*(23–24), 3322–3337. https://doi.org/10.1016/j.quascirev.2006.04.010

Prokopenko, A. A., Kuzmin, M. I., Li, H. C., Woo, K. S., & Catto, N. R. (2009). Lake Hovsgol basin as a new study site for long continental paleoclimate records in continental interior Asia: General context and current status. *Quaternary International*, *205*(1–2), 1–11. https://doi.org/10.1016/j.quaint.2009.02.031

Putnam, A. E., Schaefer, J. M., Denton, G. H., Barrell, D. J. A., Andersen, B. G., Koffman, T. N. B., et al. (2013). Warming and glacier recession in the Rakaia valley, southern Alps of New Zealand, during Heinrich stadial 1. *Earth and Planetary Science Letters*, *382*, 98–110. https://doi.org/10.1016/j.epsl.2013.09.005

Putnam, A. E., Schaefer, J. M., Denton, G. H., Barrell, D. J. A., Birkel, S. D., Andersen, B. G., et al. (2013). The last glacial maximum at 44S documented by a ^{10}Be moraine chronology at Lake Ohau, southern Alps of New Zealand. *Quaternary Science Reviews*, *62*, 114–141. https://doi.org/10.1016/j.quascirev.2012.10.034

Putnam, A. E., Bromley, G. R. M., Rademaker, K., & Schaefer, J. M. (2019). In situ ^{10}Be production-rate calibration from a 14C-dated late-glacial moraine belt in Rannoch Moor, central Scottish Highlands. *Quaternary Geochronology*, *50*, 109–125. https://doi.org/10.1016/j.quageo.2018.11.006

Putnam, A. E., Schaefer, J. M., Barrell, D. J. A. A., Vandergoes, M. J., Denton, G. H., Kaplan, M. R., et al. (2010). In situ cosmogenic ^{10}Be production-rate calibration from the Southern Alps, New Zealand. *Quaternary Geochronology*, *5*(4), 392–409. https://doi.org/10.1016/j.quageo.2009.12.001

Putnam, A. E., Schaefer, J. M., Denton, G. H., Barrell, D. J. A., Finkel, R. C., Andersen, B. G., et al. (2012). Regional climate control of glaciers in New Zealand and Europe during the pre-industrial Holocene. *Nature Geoscience*, *5*(9), 627–630. https://doi.org/10.1038/ngeo1548

Rasmussen, T. L., Thomsen, E., & Moros, M. (2016). North Atlantic warming during Dansgaard-Oeschger events synchronous with Antarctic warming and out-of-phase with Greenland climate. *Scientific Reports*, *6*(1), 20535. https://doi.org/10.1038/srep20535

Raymo, M. E., Lisiecki, L. E., & Nisancioglu, K. H. (2006). Plio-Pleistocene ice volume, Antarctic climate, and the global δ18O record. *Science*, *313*(5786), 492–495. https://doi.org/10.1126/science.1123296

Roe, G. (2006). In defense of Milankovitch. *Geophysical Research Letters*, *33*(24), L24703. https://doi.org/10.1029/2006gl027817

Roe, G. H., Baker, M. B., & Herla, F. (2017). Centennial glacier retreat as categorical evidence of regional climate change. *Nature Geoscience*, *10*(2), 95–99. https://doi.org/10.1038/ngeo2863

Rother, H., Lehmkuhl, F., Fink, D., & Nottebaum, V. (2014). Surface exposure dating reveals MIS-3 glacial maximum in the Khangai Mountains of Mongolia. *Quaternary Research*, *82*(2), 297–308. https://doi.org/10.1016/j.yqres.2014.04.006

Rother, H., Shulmeister, J., Fink, D., Alexander, D., & Bell, D. (2015). Surface exposure chronology of the Waimakariri glacial sequence in the Southern Alps of New Zealand: Implications for MIS-2 ice extent and LGM glacial mass balance. *Earth and Planetary Science Letters*, *429*, 69–81. https://doi.org/10.1016/j.epsl.2015.07.033

Rupper, S., & Roe, G. (2008). Glacier changes and regional climate: A mass and energy balance approach. *Journal of Climate*, *21*(20), 5384–5401. https://doi.org/10.1175/2008JCLI2219.1

Rupper, S., Roe, G., & Gillespie, A. (2009). Spatial patterns of Holocene glacier advance and retreat in Central Asia. *Quaternary Research*, *72*(3), 337–346. https://doi.org/10.1016/j.yqres.2009.03.007

Schaefer, J. M., Denton, G. H., Kaplan, M. R., Putnam, A. E., Finkel, R. C., Barrell, D. J. A., et al. (2009). High-frequency Holocene glacier fluctuations in New Zealand differ from the Northern signature. *Science*, *324*(5927), 622–625. https://doi.org/10.1126/science.1169312

Schaefer, J. M., Putnam, A. E., Denton, G. H., Kaplan, M. R., Birkel, S., Doughty, A. M., et al. (2015). The southern glacial maximum 65,000 years ago and its unfinished termination. *Quaternary Science Reviews*, *114*, 52–60. https://doi.org/10.1016/j.quascirev.2015.02.009

Shakun, J. D., Clark, P. U., He, F., Lifton, N. A., Liu, Z., & Otto-Bliesner, B. L. (2015). Regional and global forcing of glacier retreat during the last deglaciation. *Nature*, *6*(1), 8059. https://doi.org/10.1038/ncomms9059

Shakun, J. D., Clark, P. U., He, F., Marcott, S. A., Mix, A. C., Liu, Z., et al. (2012). Global warming preceded by increasing carbon dioxide concentrations during the last deglaciation. *Nature*, *484*(7392), 49–54. https://doi.org/10.1038/nature10915

Stone, J. O. (2000). Air pressure and cosmogenic *isotope production*, *105*(B10), 753–759. https://doi.org/10.1029/2000jb900181

Strand, P. D., Putnam, A. E., Sambuu, O., Putnam, D. E., Denton, G. H., Schaefer, J. M., et al. (2022). *^{10}Be chronology of Khoton Nuur glacial landforms since the last glaciation*. NOAA National Centers for Environmental Information (NCEI) Paleoceanography and Paleoclimatology. Retrieved from https://www.ncei.noaa.gov/access/paleo-search/study/36253

Strand, P. D., Schaefer, J. M., Putnam, A. E., Denton, G. H., Barrell, D. J. A., Koffman, T. N. B., & Schwartz, R. (2019). Millennial-scale pulsebeat of glaciation in the southern Alps of New Zealand. *Quaternary Science Reviews*, *220*, 165–177. https://doi.org/10.1016/j.quascirev.2019.07.022

Stuiver, M., & Polach, H. A. (1977). Discussion reporting of ^{14}C data. *Radiocarbon*, *19*(3), 355–363. https://doi.org/10.1017/S0033822200003672

Surazakov, A. B., Aizen, V. B., Aizen, E. M., & Nikitin, S. A. (2007). Glacier changes in the Siberian Altai Mountains, Ob river basin, (1952–2006) estimated with high resolution imagery. *Environmental Research Letters*, *2*(4), 45017. https://doi.org/10.1088/1748-9326/2/4/045017

Tierney, J. E., Zhu, J., King, J., Malevich, S. B., Hakim, G. J., & Poulsen, C. J. (2020). Glacial cooling and climate sensitivity revisited. *Nature*, *584*(7822), 569–573. https://doi.org/10.1038/s41586-020-2617-x

Toucanne, S., Soulet, G., Freslon, N., Jacinto, R. S., Dennielou, B., Zaragosi, S., et al. (2015). Millennial-scale fluctuations of the European Ice Sheet at the end of the last glacial, and their potential impact on global climate. *Quaternary Science Reviews*, *123*, 113–133. https://doi.org/10.1016/j.quascirev.2015.06.010

Windley, B. F., Kröner, A., Guo, J., Qu, G., Li, Y., & Zhang, C. (2002). Neoproterozoic to Paleozoic geology of the Altai Orogen, NW China: New Zircon age data and tectonic evolution. *The Journal of Geology*, *110*(6), 719–737. https://doi.org/10.1086/342866

Wirsig, C., Zasadni, J., Christl, M., Akçar, N., & Ivy Ochs, S. (2016). Dating the onset of LGM ice surface lowering in the High Alps. *Quaternary Science Reviews*, *143*, 37–50. https://doi.org/10.1016/j.quascirev.2016.05.001

Wirsig, C., Zasadni, J., Ivy-Ochs, S., Christl, M., Kober, F., & Schlüchter, C. (2016). A deglaciation model of the Oberhasli, Switzerland. *Journal of Quaternary Science*, *31*(1), 46–59. https://doi.org/10.1002/jqs.2831

Yabuki, H., & Ohata, T. (2009). *The recent glacier changes in Mongolian Altai Mountains*. AGU Fall Meet.

Yang, J., Chen, Y., Xu, X., Cui, Z., & Xiong, H. (2017). Quaternary glacial history of the Kanas Valley, Chinese Altai, NW China, constrained by electron spin resonance and optically stimulated luminescence datings. *Journal of Asian Earth Sciences*, *147*, 164–177. https://doi.org/10.1016/j.jseaes.2017.07.011

Zemp, M., Frey, H., Gärtner-Roer, I., Nussbaumer, S. U., Hoelzle, M., Paul, F., et al. (2015). Historically unprecedented global glacier decline in the early 21st century. *Journal of Glaciology*, *61*(228), 745–762. https://doi.org/10.3189/2015JoG15J017

Zhang, X., Li, J., Gao, M., & Jin, L. (2018). Simulated precipitation changes in central Asia since the last glacial maximum. *Quaternary International*, *490*, 82–97. https://doi.org/10.1016/j.quaint.2018.05.007

Zhang, Y., & Li, Y. (2022). Three modes of climate change since the Last Glacial Maximum in arid and semi-arid regions of the Asian continent. *Journal of Geographical Sciences*, *32*(2), 195–213. https://doi.org/10.1007/s11442-022-1942-4